NAVAL POSTGRADUATE SCHOOL
Monterey, California

AD-A274 868

‖‖‖‖‖‖‖‖‖‖‖‖‖‖‖

DTIC
ELECTE
JAN 2 5 1994
S   B   D

THESIS

A COMPARISON OF COMPUTED
AND
MEASURED TRANSMISSION DATA
FOR THE AGM-88 HARM RADOME

by

David C. Chang

September, 1993

Thesis Advisor: David C. Jenn
Second Reader: Ramakrishna Janaswamy

94-02078

‖‖‖‖‖‖‖‖‖‖‖‖‖‖‖

94 1 24 047

REPORT DOCUMENTATION PAGE		Form Approved OMB No. 0704

Public reporting burden for this collection of information is estimated to average 1 hour per response, including the time for reviewing instruction, searching existing data sources, gathering and maintaining the data needed, and completing and reviewing the collection of information. Send comments regarding this burden estimate or any other aspect of this collection of information, including suggestions for reducing this burden, to Washington headquarters Services, Directorate for Information Operations and Reports, 1215 Jefferson Davis Highway, Suite 1204, Arlington, VA 22202-4302, and to the Office of Management and Budget, Paperwork Reduction Project (0704-0188) Washington DC 20503.

1. AGENCY USE ONLY *(Leave blank)*	2. REPORT DATE 93 09 23	3. REPORT TYPE AND DATES COVERED Master's Thesis
4. TITLE AND SUBTITLE A COMPARISON OF COMPUTED AND MEASURED TRANSMISSION DATA FOR THE AGM-88 HARM RADOME		5. FUNDING NUMBERS
6. AUTHOR(S) Chang, David C.		
7. PERFORMING ORGANIZATION NAME(S) AND ADDRESS(ES) Naval Postgraduate School Monterey CA 93943-5000		8. PERFORMING ORGANIZATION REPORT NUMBER
9. SPONSORING/MONITORING AGENCY NAME(S) AND ADDRESS(ES)		10 SPONSORING/MONITORING AGENCY REPORT NUMBER

11. SUPPLEMENTARY NOTES The views expressed in this thesis are those of the author and do not reflect the official policy or position of the Department of Defense or the U.S. Government.

12a. DISTRIBUTION/AVAILABILITY STATEMENT Approved for public release; distribution is unlimited.	12b. DISTRIBUTION CODE A

13. ABSTRACT *(maximum 200 words)*

This is the continuation of the development of a computer based radome design tool. Measured electric field patterns for a AGM-88 High Speed Antiradiation Missile radome were used to validate the computer model. This computer model is based on a method of moments solution of the E-field integral equation for bodies of revolution.

14. SUBJECT TERMS Radome, Method of moments, HARM.	15. NUMBER OF PAGES 65
	16. PRICE CODE

17. SECURITY CLASSIFICATION OF REPORT Unclassified	18. SECURITY CLASSIFICATION OF THIS PAGE Unclassified	19. SECURITY CLASSIFICATION OF ABSTRACT Unclassified	20. LIMITATION OF ABSTRACT UL

NSN 7540-01-280-5500

Standard Form 298 (Rev. 2-89)
Prescribed by ANSI Std. 239-18

i

A COMPARISON OF COMPUTED
AND
MEASURED TRANSMISSION DATA
FOR THE AGM-88 HARM RADOME

by

David C. Chang
Lieutenant, United States Navy
B.S., University of Washington, 1985

Submitted in partial fulfillment
of the requirements for the degree of

MASTER OF SCIENCE IN SYSTEMS ENGINEERING

from the
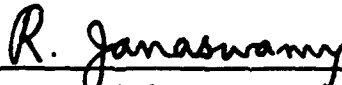

NAVAL POSTGRADUATE SCHOOL
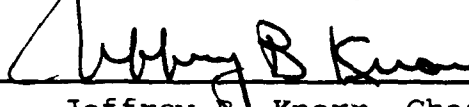September 1993

Author: _____
David C. Chang

Approved by: _____
David C. Jenn, Thesis Advisor

_____
Ramakrishna Janaswamy, Second Reader

_____
Jeffrey B. Knorr, Chairman
Electronic Warfare Academic Group

ii

ABSTRACT

This is the continuation of the development of a computer based radome design tool. Measured electric field patterns for a AGM-88 High Speed Antiradiation Missile radome were used to validate the computer model. This computer model is based on a method of moments solution of the E-field integral equation for bodies of revolution.

iii

TABLE OF CONTENTS

I. INTRODUCTION

A radome is a dome-like structure designed to provide environmental protection for an antenna. Missile radomes in particular must be designed to meet the stress of high speed flight maneuvers and aerodynamic heating. At the same time they must be able to provide suitable electrical characteristics for the antenna to receive and transmit electromagnetic waves. Nowhere is this more important than in the design of anti-radiation missile radomes. These missiles must counter a wide frequency spectrum of threats, thus requiring radomes with broadband electrical characteristics. However, due to the severe structural requirements, the electrical characteristics generally become a secondary priority in the design.

Most radomes for missile applications are based wholly or in part on the ogive shape. The electrical design of a curved radome is complicated because of the many possible transmission paths through the radome due to reflections. Ray tracing, as illustrated in Figure 1.1, is commonly used to analyze radome performance, but this method becomes tedious and inaccurate when higher-order reflections are present. Ray tracing models also assume a radome curvature large enough so that the surface can be considered locally flat. Furthermore, ray tracing techniques assume the radome is in the far field

1

of the antenna which is not necessarily the case in practice.
As a result, ray tracing techniques are not the most accurate
models to use in analyzing the performance of an antenna with
a radome.

ray tracing techniques
assume rays are
parallel and that the
scattering surface
is locally flat.

defocussing
due to
curvature of
the radome.

antenna

radome curvature
is not large
enough to be
considered
locally flat.

rays are
not
parallel
in the
near
field.

tangential vectors
on the surface
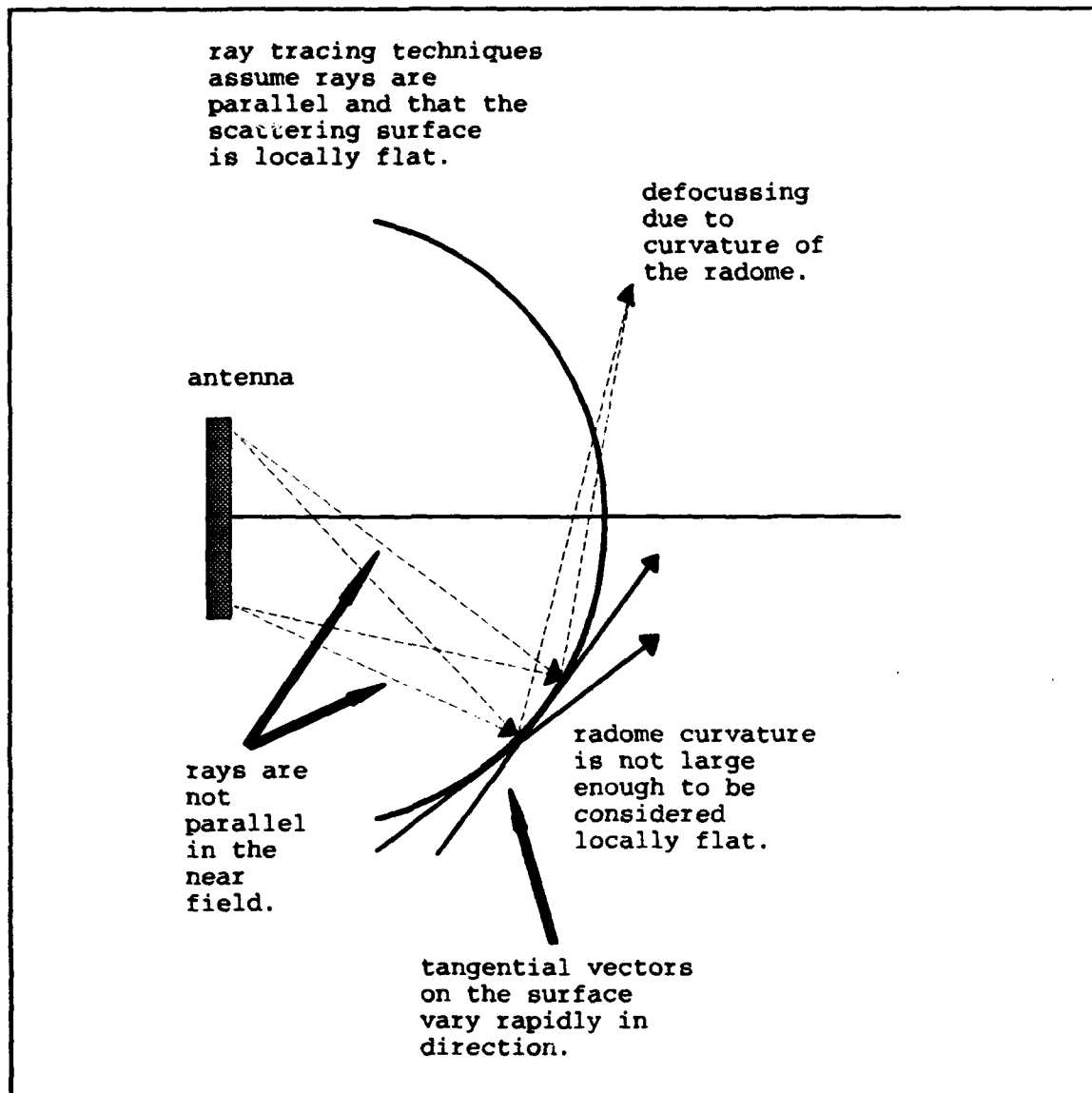vary rapidly in
direction.

Figure 1.1 Radome ray tracing approximations. [After Ref.1]

The method of moments(MM) is a solution to an integral equation that is rigorous in principle. It includes multiple reflections, surface waves, and can handle radomes in the near-field of the antenna. A MM computer code was developed by Francis [Ref. 1] and improved by Klopp [Ref. 2]. The code was verified for simple radome shapes with single-layer walls, but has not been used to model multilayer walls. It is the objective of this thesis to compare measured and computed results for a multi-layer radome designed for use by a modern anti-radiation missile (ARM). Verification of the code with measured data will allow it to be used with confidence in the design process, with a potential savings of time and money.

Chapter II discusses the history and development of the ARM and includes a brief explanation of its seeker and the required radome characteristics.

Chapter III explains the basic elements of radome design. Aerodynamic considerations will be discussed and the various tradeoffs that must be considered in the design are addressed. The geometry of an ogive radome will also be illustrated and explained.

In Chapter IV, a description of the antenna measurement facility, the test procedure, and measured VSWR using the HP 8510 network analyzer will be discussed.

Concurrent with the hardware testing, computer modeling was performed using the simulation developed by Francis [Ref. 1] and Klopp [Ref. 2]. The theory behind this simulation is

derived in Chapter V. This simulation provides pattern and gain estimates as a function of radome parameters and geometry. It is based on a method of moments solution of the electric field integral equation for bodies of revolution(BOR) developed by Mautz and Harrington [Ref. 3]. An important capability of the code is that the radome can be located in the near field of the antenna.

Chapter VI presents the measured data from both the hardware measurements and the computer simulation. Finally Chapter VII will present some conclusions and guidelines for radome design based on the measured and computed results.

II. BACKGROUND

A radome is designed to protect the antenna, but not to interfere with its operation. Radome performance thus depends on the material used in the construction. Initial radome design in the 1940's incorporated plywood as the radome material. However, this material proved to be unsatisfactory due to its high moisture absorption in wet weather and the resulting degradation in electronic transmissions. Fabric reinforced resins were then developed and exhibited good electrical properties. The one drawback to using resins was their poor resistance to physical stress. In order to increase the strength-to-weight ratio early designers simply increased the thickness of the material. However, the importance of maintaining thin radome walls with respect to the radome wavelength to minimize radome wall reflections was not appreciated at the time. This was clearly illustrated by the U.S. "pathfinder" program. The poor performance of a radar equipped bomber to guide bomber formations to the target almost doomed the program in its genesis. Problems such as this clearly indicated that there was a need for a rational and generalized theory of electrical design for future radomes. [Ref. 4: pp. 1-3]

Today there is an even greater need for an understanding of a radome and its ability to act as a window for an antenna.

The advent of radar guided missiles meant that radomes had to meet the physical stresses of high speed flight, while at the same time providing optimal electrical performance. Nowhere is this more important than in a high speed anti-radiation missile, which is designed to seek out and destroy radar antennas by homing in on their emitted RF energy.

A. HISTORY OF ANTI-RADIATION MISSILES

Historically, the first effective use of an anti-radiation missile (ARM) occurred during the Vietnam conflict. The two missiles that were widely used during this period were the AGM-45 Shrike and the AGM-78 Standard ARM. These two missiles had only limited success due to their narrow frequency coverage and enemy tactical countermeasures. Efforts to improve these systems resulted in the High Speed Anti-radiation Missile (HARM).

1. THE AGM-45 SHRIKE

The Shrike (Figure 2.1) is a medium range first generation ARM that entered service in the mid - 1960s. Its development was directly in response to the growing radar guided missile threat in Vietnam. On board aircraft ESM/ECM receivers provide initial warning of illumination by ground defense radars. Once acquisition of the radar is achieved by the missile warhead it is then fired. Guidance is accomplished by passive radar homing using one of twelve different homing head assemblies set to a specific frequency

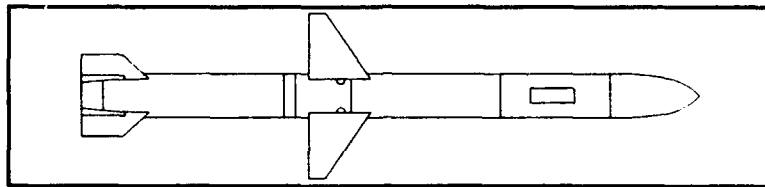range. It was highly successful in Vietnam, the Middle East, and in the U.S. Navy Libya strikes in 1986.

Figure 2.1. AGM-45 Shrike.

2. THE AGM-78 STANDARD ARM

The Standard ARM (Figure 2.2) was developed in the late 1960s and is an air launched version of the RIM-66 Standard surface-to-air missile. It has increased range and a larger warhead than Shrike, and contains a single homing assembly programmed by the aircraft operator.
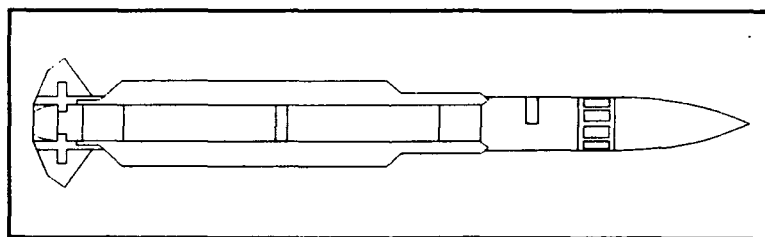

Figure 2.2. AGM-78 Standard ARM.

3. THE AGM-88 HARM

The HARM (Figure 2.3) is a second generation ARM designed to replace both the Shrike and the Standard ARM. The main improvements incorporated included a broadband antenna, higher speed, programmable software, and increased frequency

range. Unlike Shrike, HARM uses a single warhead with a broadband capability. This allows the missile to operate against a large number of RF threats. Its software controlled processing gives it the ability to be reprogrammed in the field as opposed to using hardware modifications in the missile as enemy weapons develop. The seeker head employs a fixed antenna that greatly simplifies the design and cost. The seeker head is comprised of the antenna array, ten microwave circuit boards and a video processor. This configuration provides direction finding capability without the need for a moving gimballed assembly. The antenna array consists of a plane spiral helix with other elements within a radome which itself forms an integral part of the overall RF antenna system. This missile is capable of being carried by a wide range of aircraft and is used by both the U.S. Navy and Air Force. [Ref. 5]
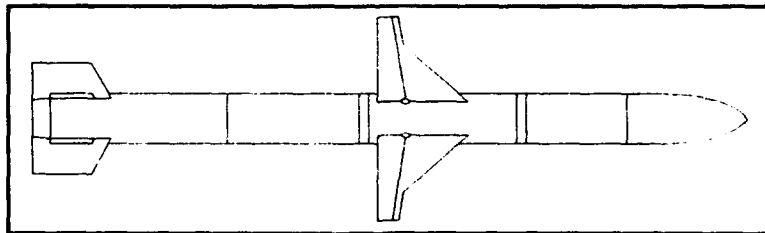

Figure 2.3. AGM-88 HARM.

B. THE ANTI-RADIATION SEEKER

The ARM seeker passively detects the power emitted from the victim radar. The power received at the antenna is given by the radar equation

$$P_r = \left(\frac{\lambda}{4\pi R}\right)^2 G_t G_r P_t .$$
(2.1)

P_t is the transmitter power, R is the range from the target transmitter to the anti-radiation missile seeker receiver, and G_t and G_r are the gains of the transmitter and receiver antennas. In practice, the radome introduces an additional loss in gain relative to the antenna in free space. [Ref. 3: p. 18]

The seeker design is both challenging and difficult as it must cover an extremely wide frequency range. ARM seekers must also have the ability to lock on to both the side and back lobes of the victim radar. The ARM is guided to the proximity of the victim radar by guidance signals generated by the antenna, processing circuitry, and computational equipment. The antenna is a crucial part of the seeker system because it provides the radar signals which are then processed to determine angle of arrival. However, the antenna information can potentially be distorted by the radome that protects it. Only a few radar signal parameters are used by the seeker to sort and classify the threat pulse radars by type. [Ref 6: pp. 18-24]

III. RADOME DESIGN

Broadband, multi-octave frequency coverage is a challenging requirement in the design of the modern ARM seeker. It allows the seeker the flexibility to scan all the frequencies that the target radar will radiate. As a result, the radome of the missile must be able to operate over the same frequency range of the target emitters. The transmission requirements for a radome on a passive radiation sensing missile are not as demanding as compared to the requirements for an active or semi-active radiation sensing missile for equal range performance and moderate power transmitter capabilities. Unlike the active or semi-active systems the passive seeker on an anti-radiation missile operates on a much higher signal-to-noise ratio. For the active and semi-active systems, if maximum range is the design goal then the radome must pass at least 90% of the incident energy. This is due primarily to the low signal-to-noise ratio that these seekers must work with. The passive sensor, however, can operate with a radome that has up to 50% transmission loss. [Ref. 7: p.16]

A. AERODYNAMIC CONSIDERATIONS

Radome design is generally dictated by aerodynamic considerations. Reduction of drag is of prime importance when considering speeds more than Mach 1. The composition of the

10

radome material plays a key role in determining aerodynamic heating, dynamic pressure, and rain erosion. The ideal electrical shape for a missile is a hemisphere, however a long and slender shape is the best aerodynamically for a missile. A compromise must therefore be reached in which the aerodynamic shape does not degrade the electrical performance of the radome. [Ref. 7: pp. 1-4]

B. RADOME ELECTRICAL CHARACTERISTICS

RF energy transmitted through the radome is a function of shape, frequency, wall construction, incident angle, and polarization. Given aerodynamic constraints, the only parameter that can change in the design is wall construction. The number of layers, the dielectric constant of each layer, and the thickness must be taken into account in the design of the radome wall.

Single material radomes are the most common radomes found. The thickness of these radomes is adjusted so that it is close to one-half the wavelength of the electromagnetic wave propagating in the material at the frequency of interest. This condition minimizes multiple reflections on the inside of the material. These radomes provide good phase characteristics and high transparency. However, at low frequencies $\lambda/2$ may be too thick to be practical, whereas at high frequencies it may be too thin.
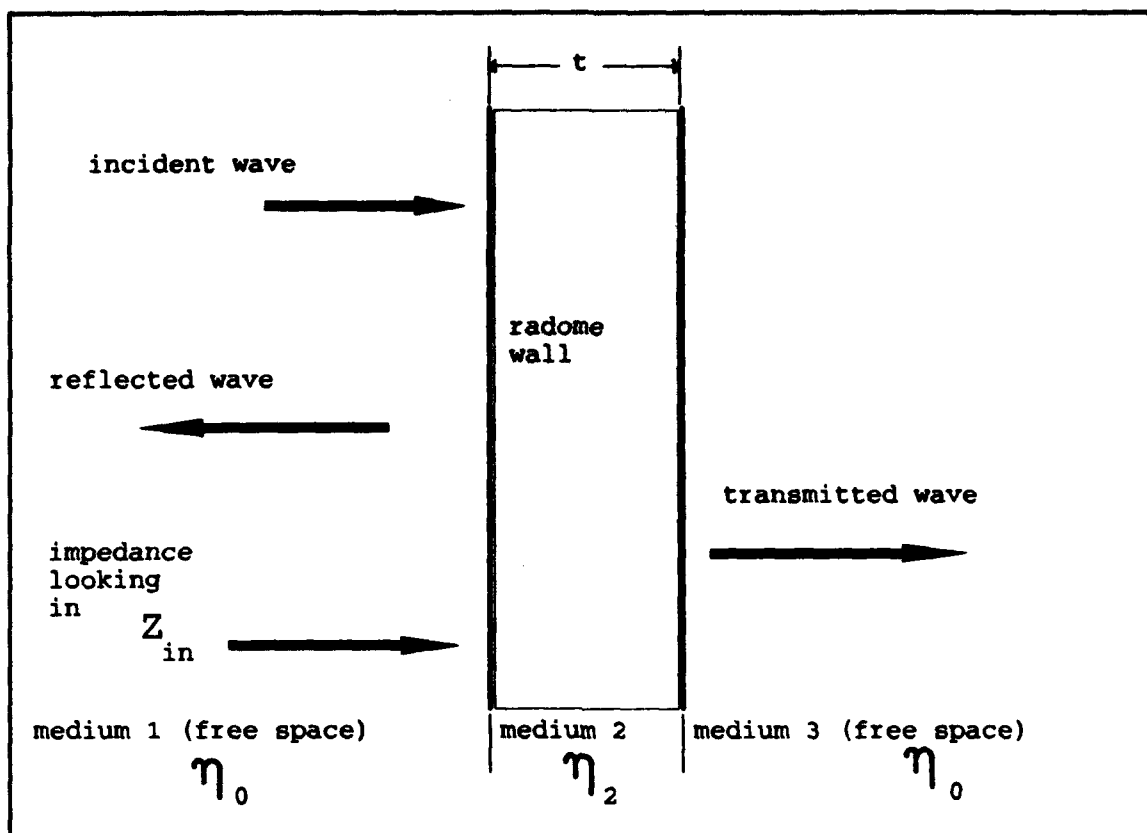
Figure 3.1 Single boundary layer.

A crude estimate of the reflection loss (Figure 3.1) due to the radome is given by the plane wave reflection-coefficient at an air/dielectric interface. The intrinsic impedance of media 1 and 3 is η_0, and the intrinsic impedance of medium 2 is η_2. The impedance looking into the radome is denoted Z_{in}. The reflection coefficient seen by an incident wave is

$$\rho = \frac{Z_{in} - \eta_0}{Z_{in} + \eta_0} .$$ (3.1)

12

Large reflections are produced when Z_{in} is significantly different than η_0 . All the energy is transmitted when Z_{in} is equal to η_0.

In practice the reflection from the second boundary is important and has significant effect on the value of Z_{in}. For a given incidence direction, frequency can be chosen so that the reflection from the second surface will cancel with the reflection from the first surface. This is referred to as a tunned radome, but this method is only effective over a narrow frequency range. An example of transmission through a tunned radome is shown in Figure 3.2.
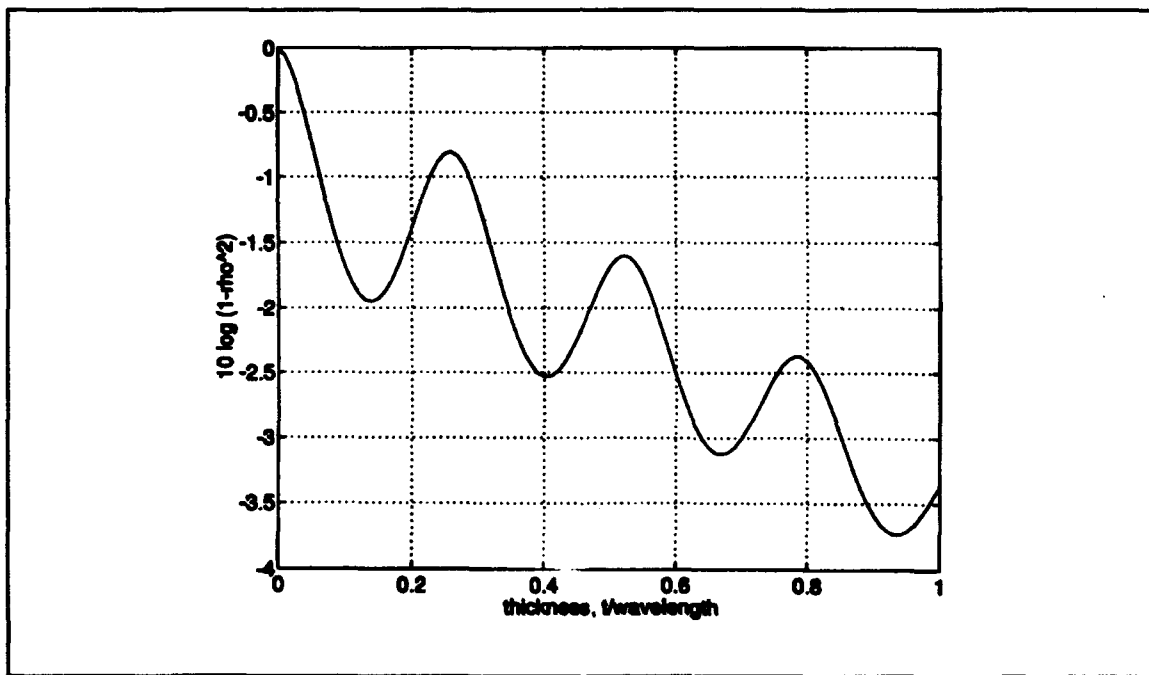

Figure 3.2 Transmission through a tunned radome. Dielectric constant of material $\varepsilon_r = 3.5$, reflection coefficient $\delta = .05$, and incidence angle $\theta_i = 0$.

13

Using impedance matching, broadband transmission can be achieved for the radome. The outside layer of the radome is constructed of a material with a low dielectric constant. Each subsequent layer has a higher dielectric constant than the previous layer. This creates essentially a tapered transmission line as illustrated in Figure 3.3.[Ref. 7: pp. 16-18]
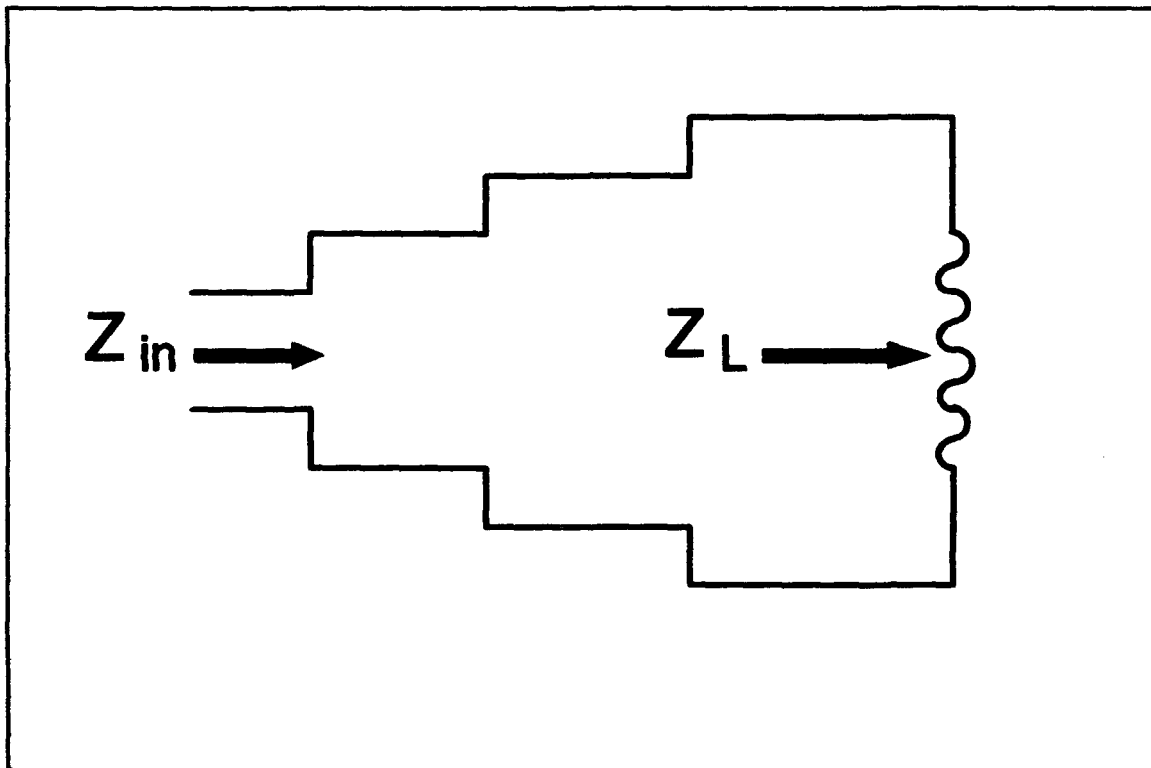

Figure 3.3 Stepped impedance transformer. [From Ref. 7]

Another technique in designing the wall of the radome is to alternate the layers of low and high dielectric constant material as shown in Figure 3.4. There are several types of laminated walls that employ this technique of alternate

14

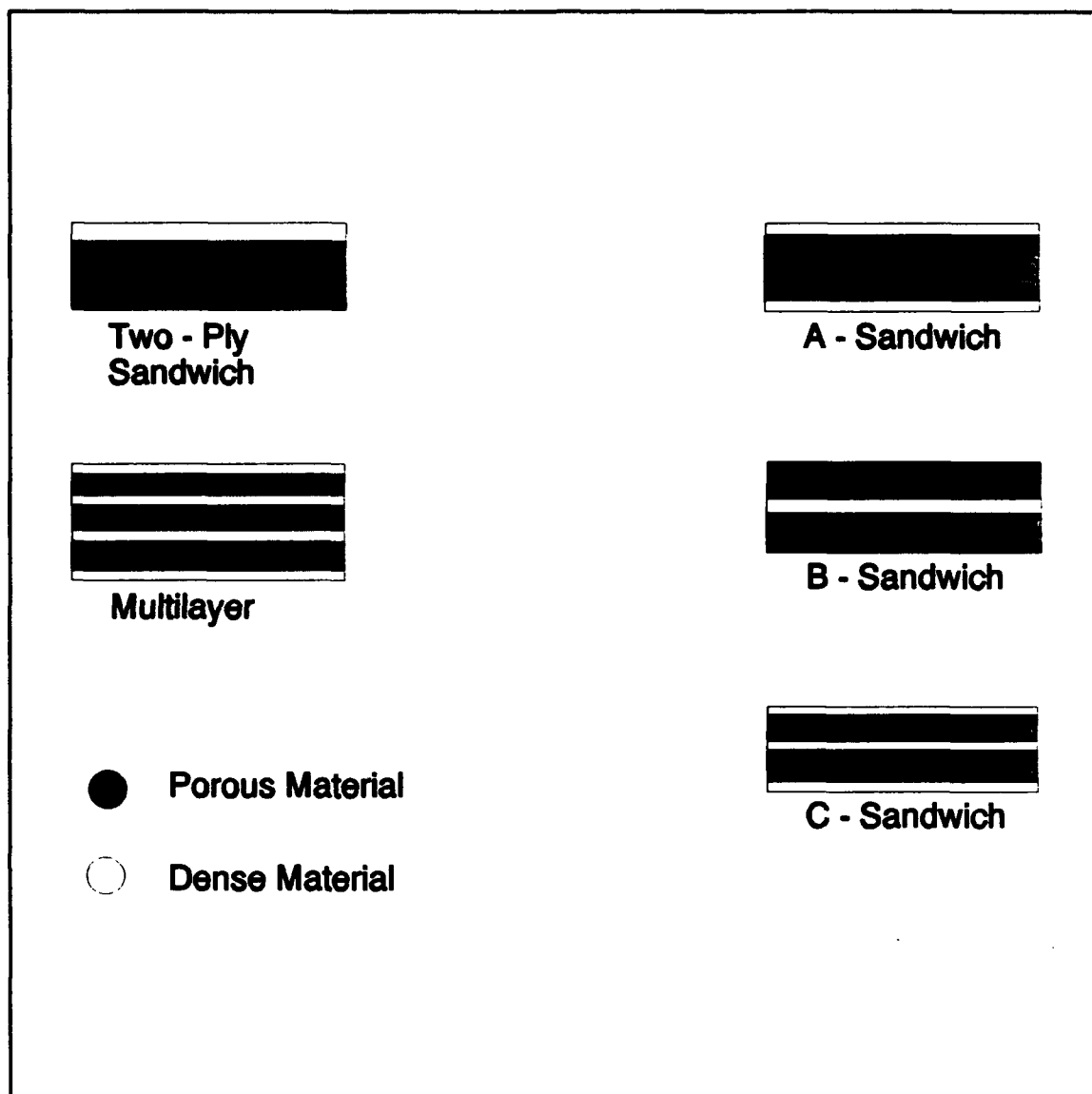**Figure 3.4** Laminate radome material.

layers. The first is the two-ply sandwich which is composed of a high dielectric material on the outside with a low dielectric material on the inside. However, this simplest form of lamination is mainly advantageous at low frequencies.

One of the most frequently used multi-layer designs is the A-sandwich. It is composed of a low dielectric core with a

15

thin skin of denser material on both sides. It provides a rigid structure with good strength-to-weight ratio and broadband capabilities.

The B-sandwich is a single layer of high dielectric material sandwiched between two low dielectric materials. A design with the weaker low dielectric material on the outside is generally not used. The low tolerance of the exterior material to in-flight stress and environmental conditions are the main drawbacks despite its being superior to the A sandwich electrically.

The C-sandwich consists of multiple layers of low and high dielectric material. This design is inherently structurally rigid and is used where broadband capabilities, as in an ARM radome, are the prime consideration. Plastic laminates are used for the different layers providing the high degree of strength required. [Ref. 4: pp. 44-47]

The radome to be used for the gain and pattern comparison is an AGM-88 HARM radome. This radome has a slightly modified ogive shape with an A-sandwich wall construction having an the inner core made from a soft honeycomb. This composition of the radome wall offers broadband capabilities to the seeker. The nominal thickness and dielectric constants of the HARM radome are illustrated in the Figure 3.5. [Ref. 8: pp. 1-5]

1. DETERMINING MULTILAYER RADOME IMPEDANCE

$\mathbf{\mathcal{E}}_r = 3.5 \qquad 1.2 \qquad 3.5$

exterior

Honey-
comb

interior

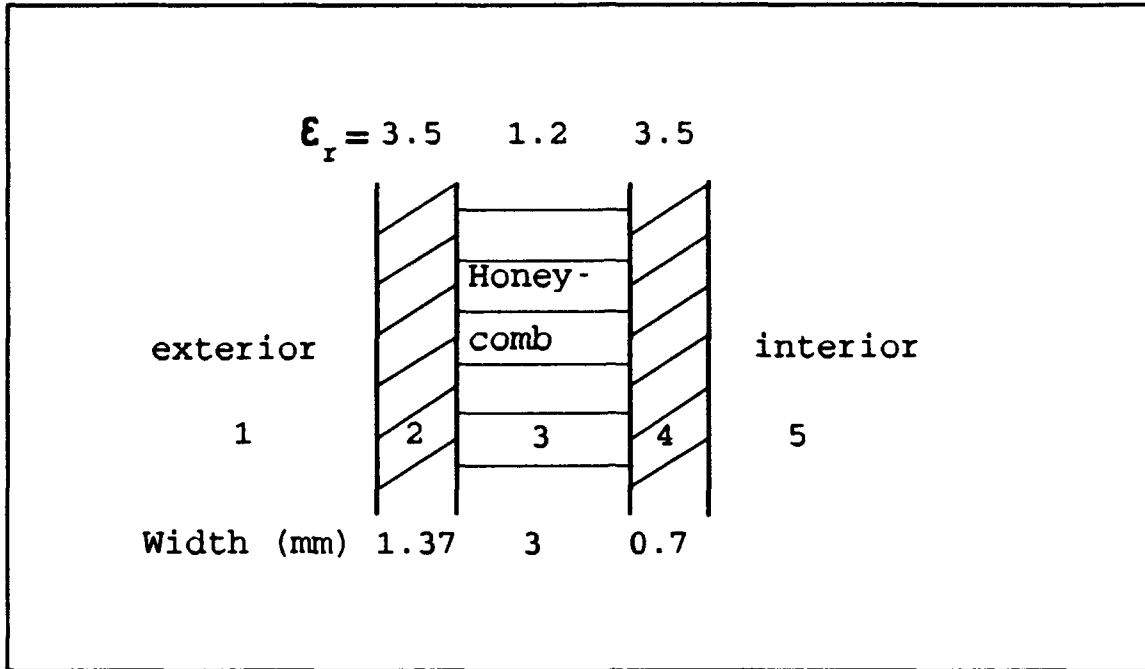1   2   3   4   5

Width (mm) 1.37   3   0.7

Figure 3.5   HARM radome wall construction.

From Figure 3.5 it can be seen that each layer of the
radome has a different dielectric constant. The transmission
line equivalent illustrated in Figure 3.3 can be applied to
this multi-layer radome. Let η_i be the intrinsic impedance of
the region i as defined in Figure 3.5, and Z_i be the impedance
looking into the region i (at the boundary between the regions
i and $i{+}1$). Using this notation, the impedance Z_i for normal
incedence is

$$Z_i = \eta_i \left[\frac{Z_{i+1} + j\eta_i \tan(\beta_i t_i)}{\eta_i + j Z_{i+1} \tan(\beta_i t_i)} \right] \qquad 2 \le i \le 4 \quad . \tag{3.2}$$

In equation (3.2)

$$\eta_i = \sqrt{\frac{\mu_o}{\epsilon_{r_i}\epsilon_o}} \qquad (3.3)$$

$$\beta_i = \omega \sqrt{\mu_o\epsilon_o\epsilon_{r_i}} \qquad (3.4)$$

and t_i is the thickness of section i.

The radome interior is region 5 and the exterior region 1. The input impedance seen by a wave from the exterior region is computed by transforming the "free space" load of the interior back to the exterior surface. An input impedance is computed at each interface and then used as a load to be transferred back to the previous interface. This is repeated until Z_{in} is computed for the final outer layer. The impedance looking in Z_{in} ($Z_{in} = Z_2$ in the notation of equation (3.2)), is then used to solve for the reflection coefficient using equation (3.1). Note that an equivalent single layer radome could be determined from the equation

$$Z_{in} = \eta_e \left[\frac{\eta_0 + j\eta_e \tan(\beta_e t_e)}{\eta_e + j\eta_0 \tan(\beta_e t_e)} \right] . \qquad (3.5)$$

Since Z_{in} is complex there is enough information to solve for both η_e and $\beta_e t_e$. [Ref. 9: pp. 454-467]

C. OGIVE GEOMETRY

The most common shape used in the design of missile radomes today is the ogive shown in Figure 3.6. The ease of

18

fabrication and acceptable high speed performance make this a popular shape. The ogive is a segment of a circle with a radius (**R**) larger than the base radius (**b**) of the radome. The curve generated for the radome is rotated around the missile axis (**z**) forming a body of revolution (BOR). The ogive shape is given by the equation

$$r = \sqrt{R^2 - z^2} + b - R .$$ (3.2)
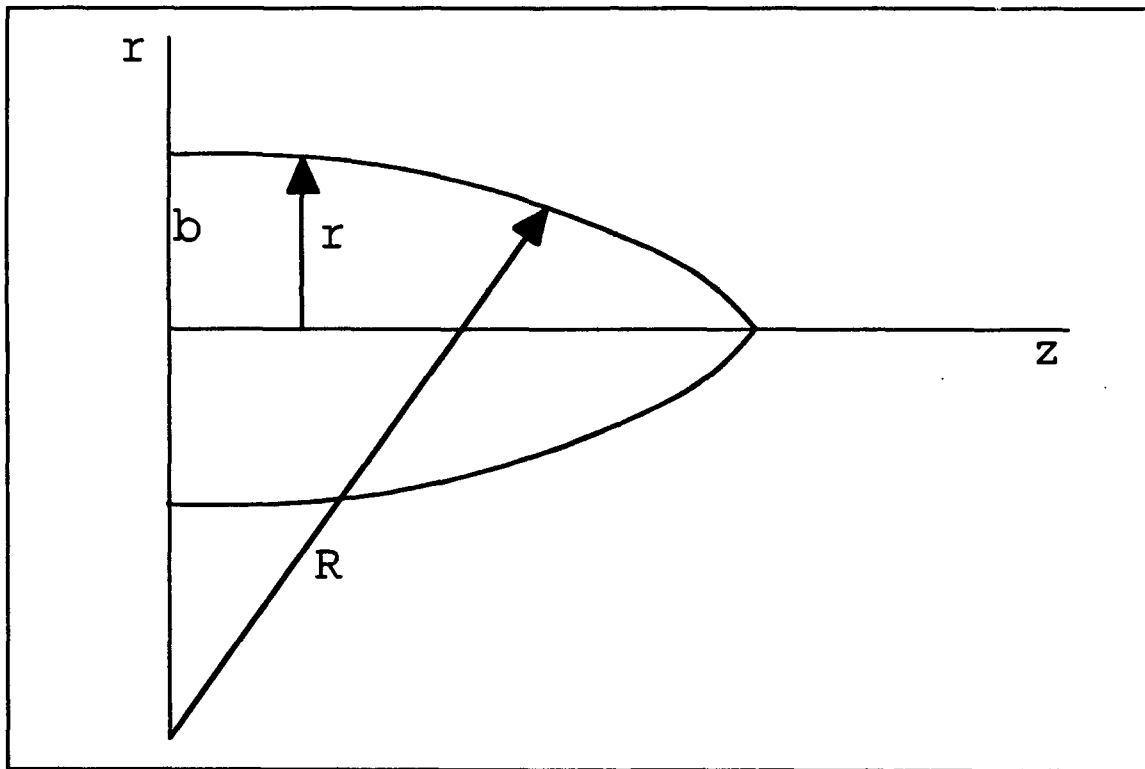
[Ref. 4: pp. 47-48]

Figure 3.6 Ogive geometry. [After Ref. 1]

The curve of the HARM radome analyzed in this thesis is not a pure ogive, but a composition of four different curves

19

as shown in Figure 3.7. The radius r is a function of the coordinate z as follows:

Segment A: $r_A = (.7002z) + .13$ **(3.3)**

Segment B: $r_B = 1.312\sqrt{(z - 0.692)}$ **(3.4)**

Segment C: $r_C = \sqrt{(21.7964)^2 - (z - 11.3988)^2} - 18.1152$ **(3.5)**

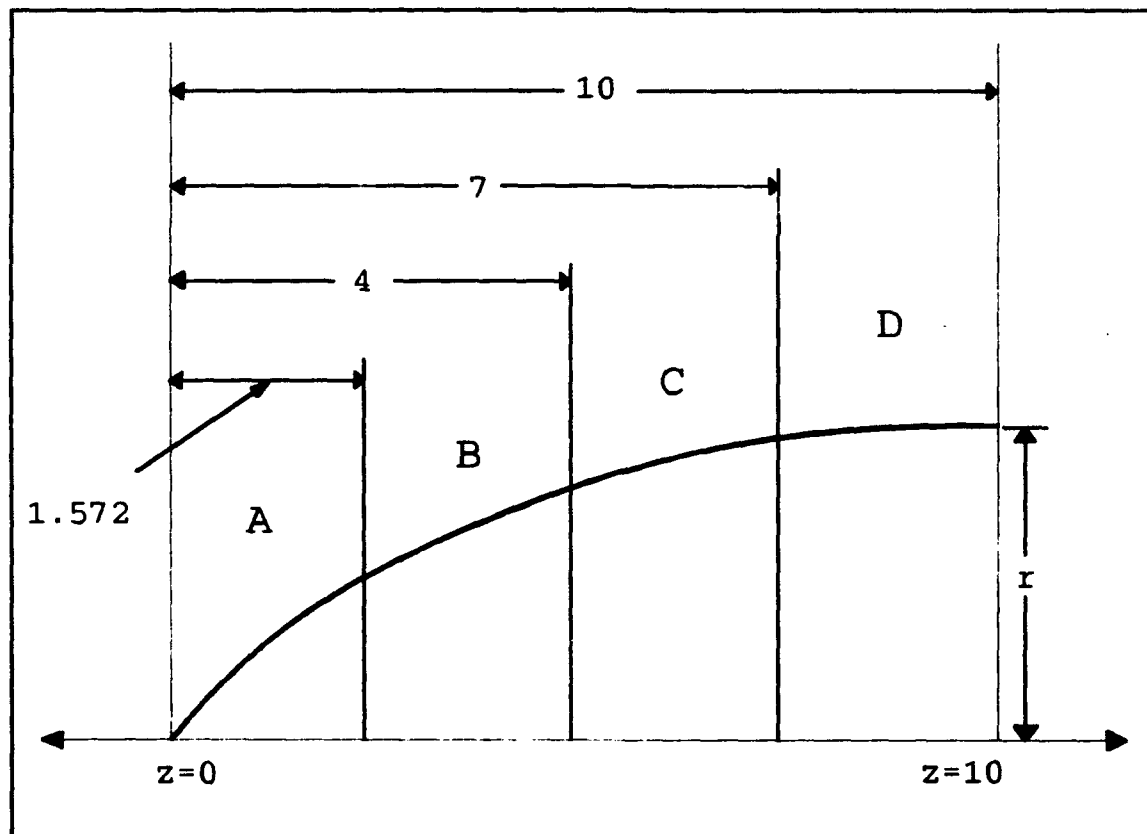Segment D: $r_D = \sqrt{(213.1228)^2 - (z - 36.1048)^2} - 207.8924$ **(3.6)**

Figure 3.7 HARM radome segments, where 1 unit is approximately 2.05 cm.

20

As shown in Figure 3.8 an ogive with R = 17 closely matches the actual HARM radome curve. This approximation will be used in the computer simulation for convenience. [Ref.8: pp. 1-5]
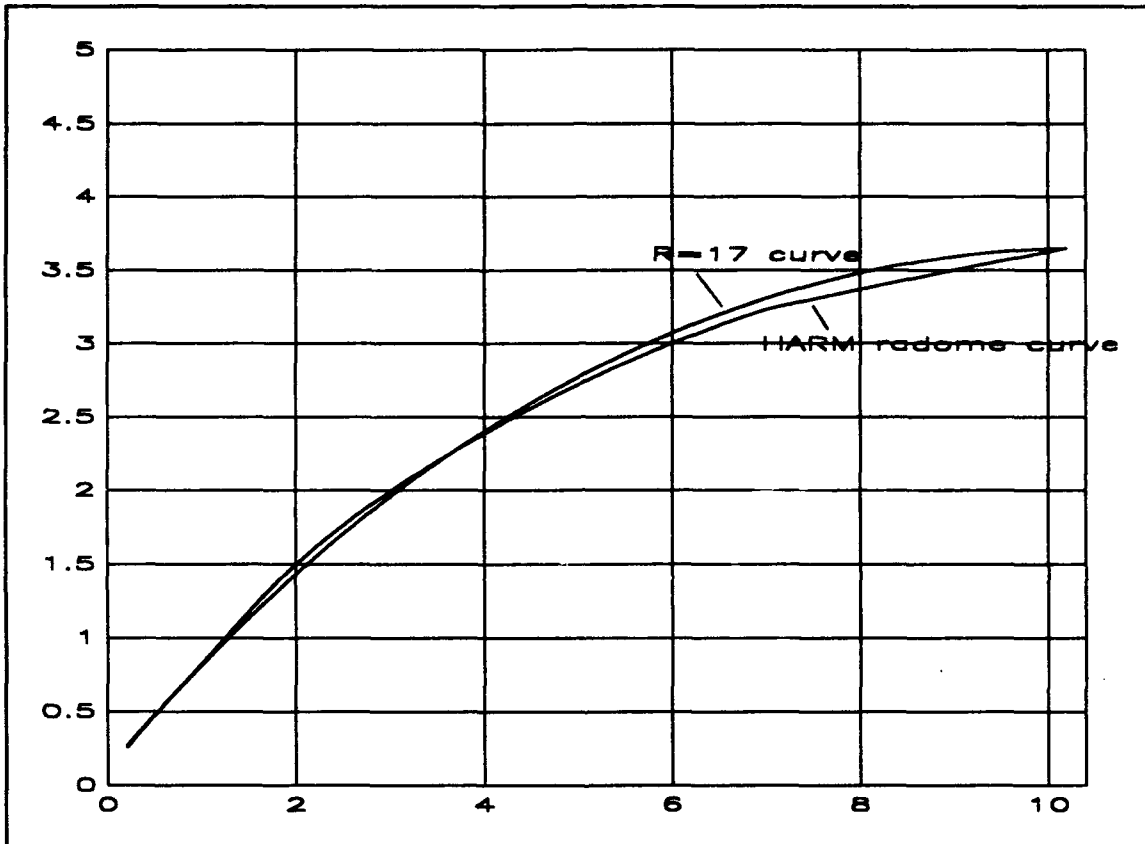

Figure 3.8 Plot of the ogive curve with R = 17 and the HARM ogive curve using equations (3.3 - 3.6).
1 unit = 2.05 cm.

IV. PATTERN, GAIN AND VSWR MEASUREMENT

A. PATTERN AND GAIN MEASUREMENT

Rectangular horn antennas were used for both transmit and receive in the test setup. The radome patterns and gain measurements were performed in an anechoic chamber. The chamber is an enclosed room whose walls are lined with microwave absorbing material to suppress reflections and therefore simulate a free space environment. Absorbers are shaped in the form of wedges or pyramidal cones to enhance absorption of the incident wave through a gradual transition from free space into the lossy absorbing material, thus providing very low reflection.

1. TEST SETUP AND INSTRUMENTATION DESCRIPTION

An HP X890A was used as the transmitting antenna, and a Microline 56X1 as the receiving antenna. The Microline 56X1 is a standard gain antenna capable of receiving frequencies in X band. The dimensions for both antennas are given in Figure 4.1.

The 56X1 was mounted on a rotating pedestal and the transmitter tuned to an X band frequency (8.0 to 12.0 GHz). The signal received by the rotating test antenna is detected and is used to drive a chart recorder which plots the test antenna pattern. The "E-plane" is defined by the orientation
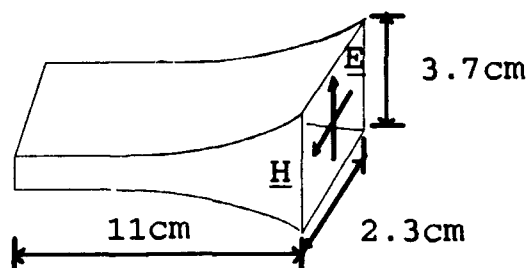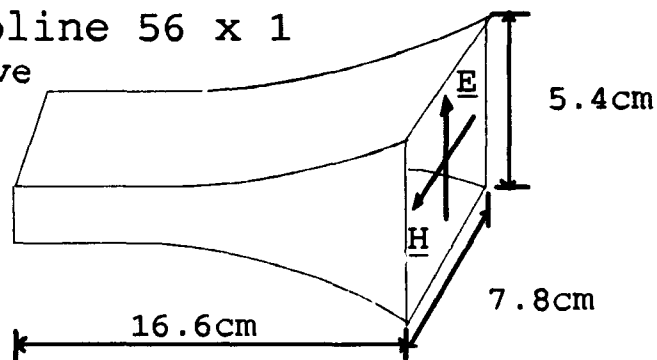
Figure 4.1 The 56X1 and HP X890A horn antenna dimensions.

of the electric field vector in the horn aperture as identified in Figure 4.1. The H-plane is orthogonal to the E-plane. They are also referred to as vertical and horizontal planes, respectively, since these are the orientation of the electric field with respect to the chamber floor. A diagram

of the anechoic chamber test equipment is illustrated in Figure 4.2.
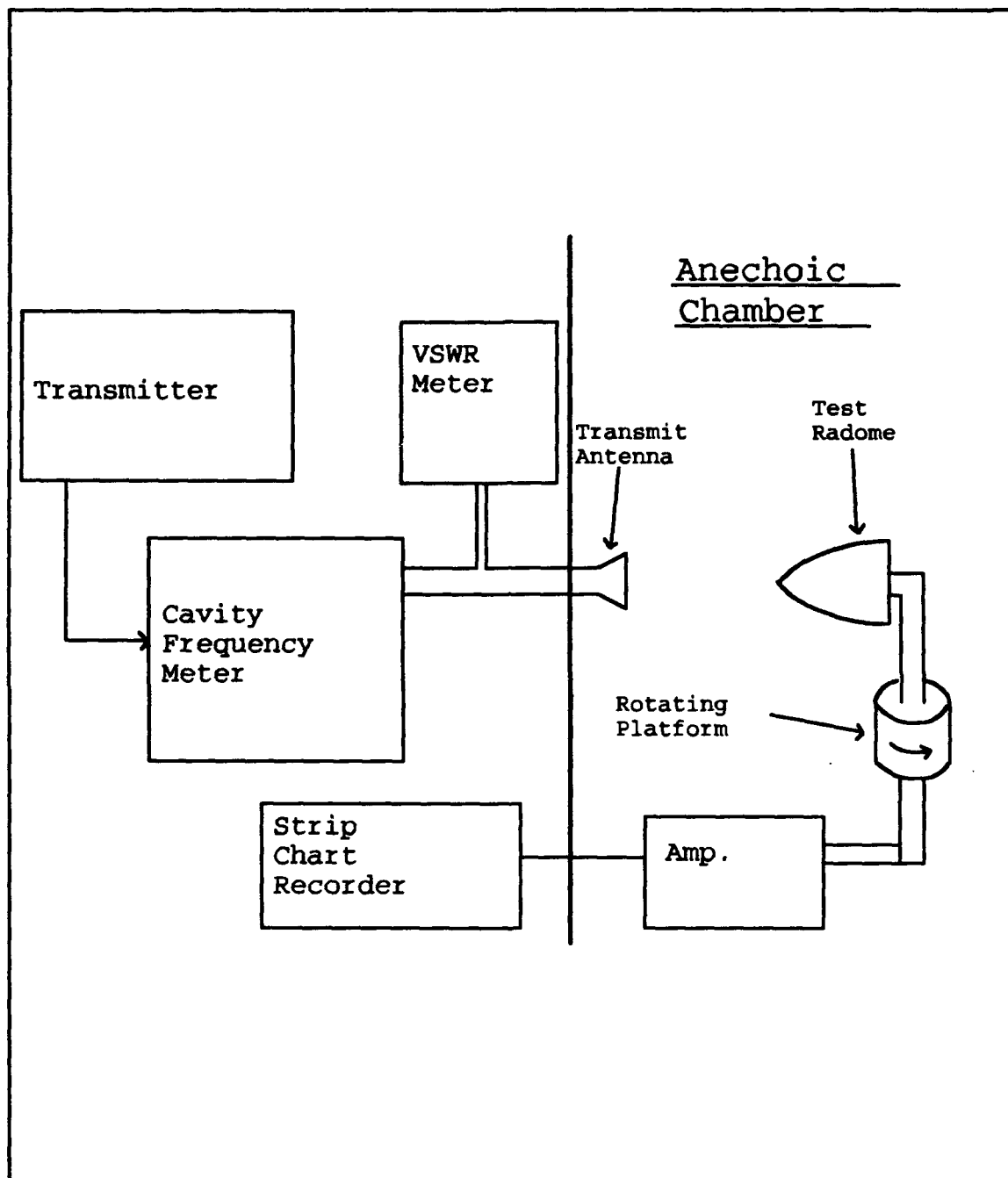
Figure 4.2 Anechoic chamber test setup.

B. VSWR MEASUREMENT

VSWR measurements for the 56X1 and the HARM radome were done using a HP8510 network analyzer shown in Figure 4.3. The network analyzer consists of a sweeper or synthesizer to provide the RF signal source. The test set provides signal separation and the first frequency conversion stage. The HP8510 consists of two instruments, the IF/Detector and the Display/Processor. The system components are controlled by a dedicated bus allowing the HP8510 to take full advantage of the capabilities of the various instruments. [Ref. 10: pp. (3-1)-(3-8)]

Figure 4.3 The HP 8510 Network Analyzer. [From Ref. 10]

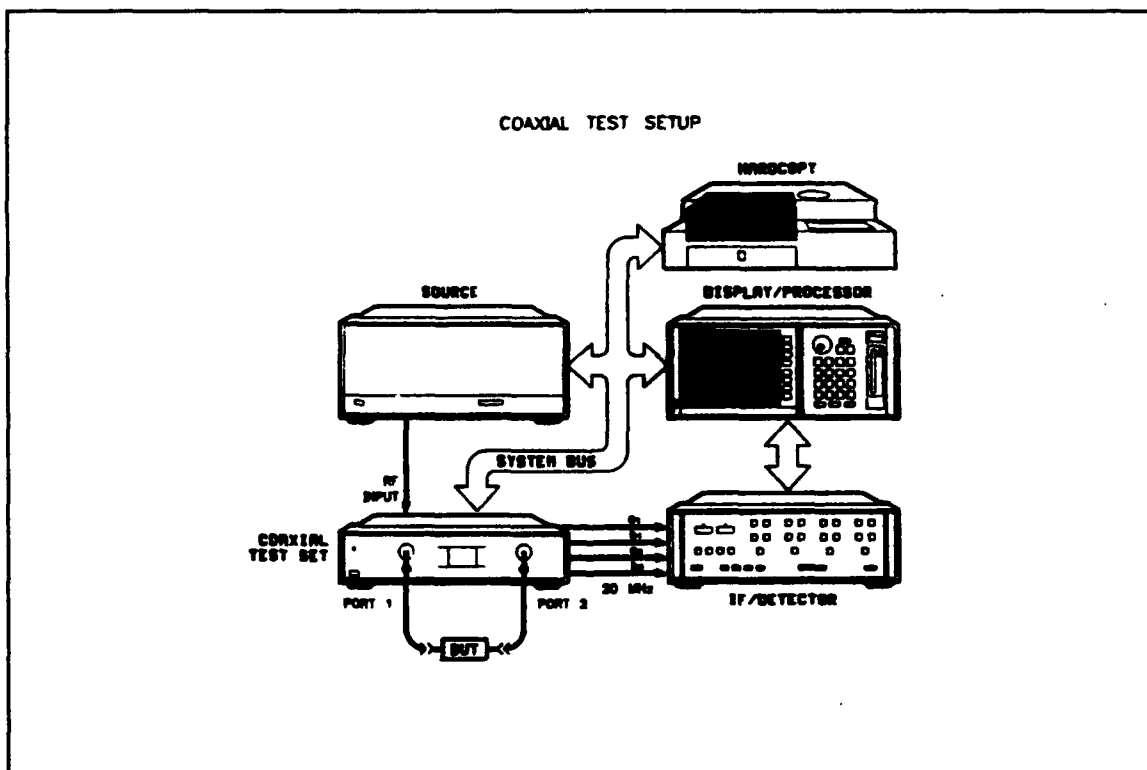A test set provides the points at which the device under test is connected, and provides signal separation to measure the four S-parameters. First the network analyzer was used to measure the reflection magnitude and phase of the isolated antenna. Next the radome was installed in front of the antenna and the measurement repeated. A comparison of the two identifies the effect of the radome on the antenna VSWR. The measured VSWR for the 56X1 was obtained after first calibrating the network analyzer for a 1 port device. VSWR measurement is calculated from the return loss by

$$\rho = 10^{D}, \tag{4.1}$$

$$SWR = \frac{(1+\rho)}{(1-\rho)}, \tag{4.2}$$

where D is the measured return loss value in dB divided by 20. [Ref. 10: pp. (10-1)-(10-4)]

The manufacturer VSWR specification for the 56X1 is 1.15. The VSWR as measured on the network analyzer is shown in Figure 4.4 for X-band frequencies. For the antenna with the radome in front, the measured VSWR is shown in Figure 4.5. The maximum VSWR is essentially unchanged with the radome present.

Figure 4.4 Measured VSWR of the 56X1 antenna.
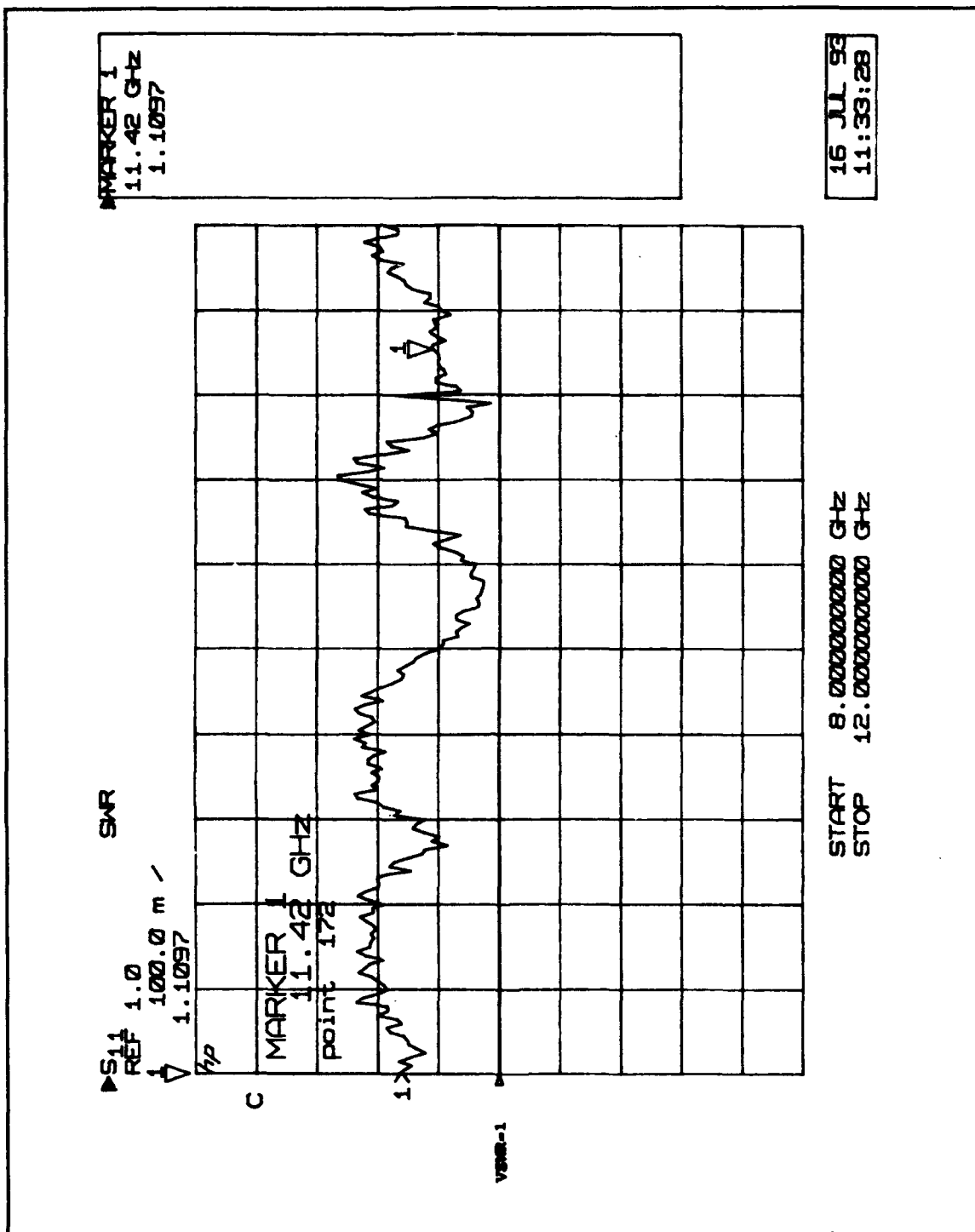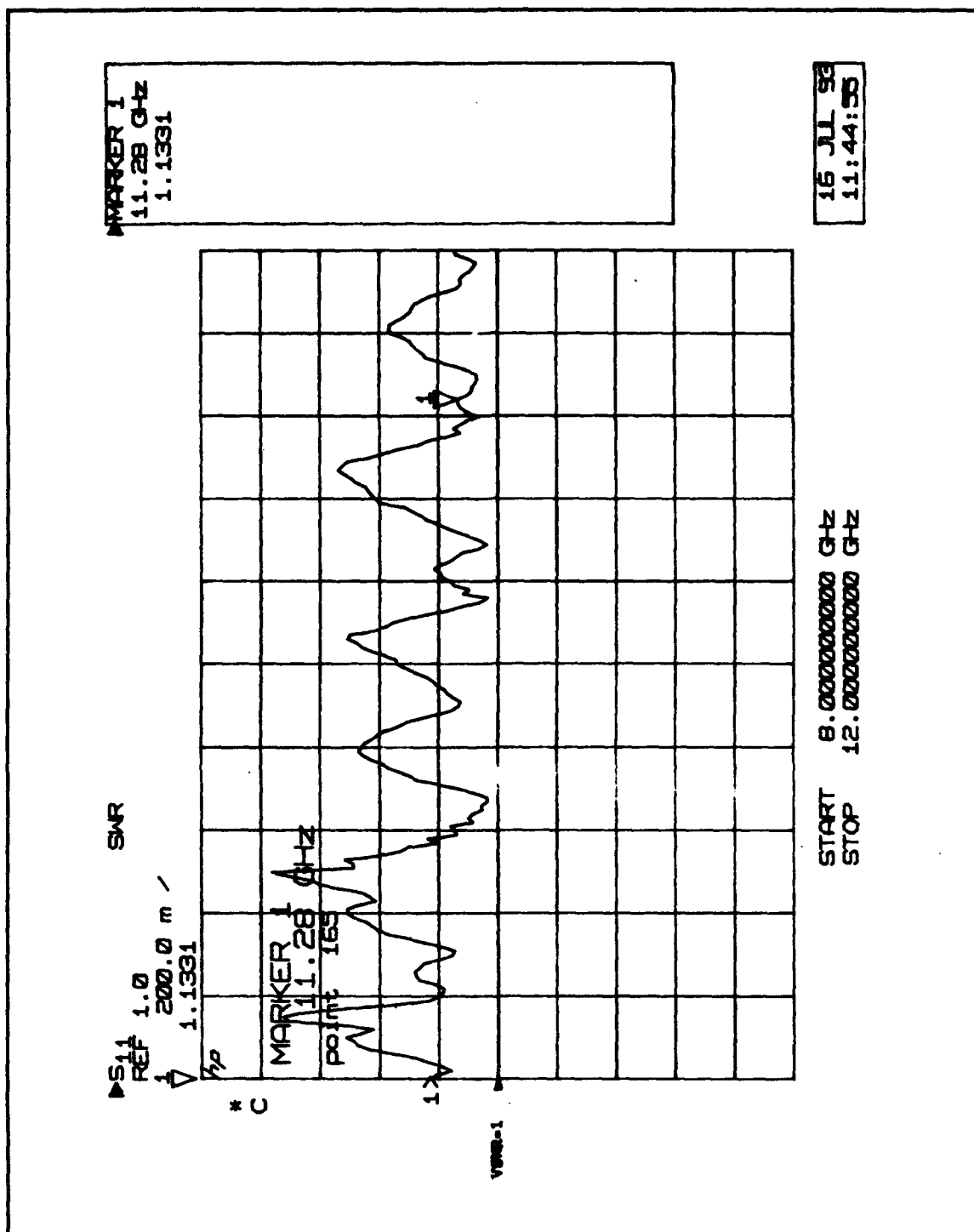
27

Figure 4.5 Measured VSWR of the 56X1 antenna and HARM radome.

V. METHOD OF ANALYSIS

The objective of this work is to validate the computer code by comparing computed and measured patterns and gain data for the antenna and radome. The antenna and radome are defined in the spherical coordinate system shown in Figure 5.1.
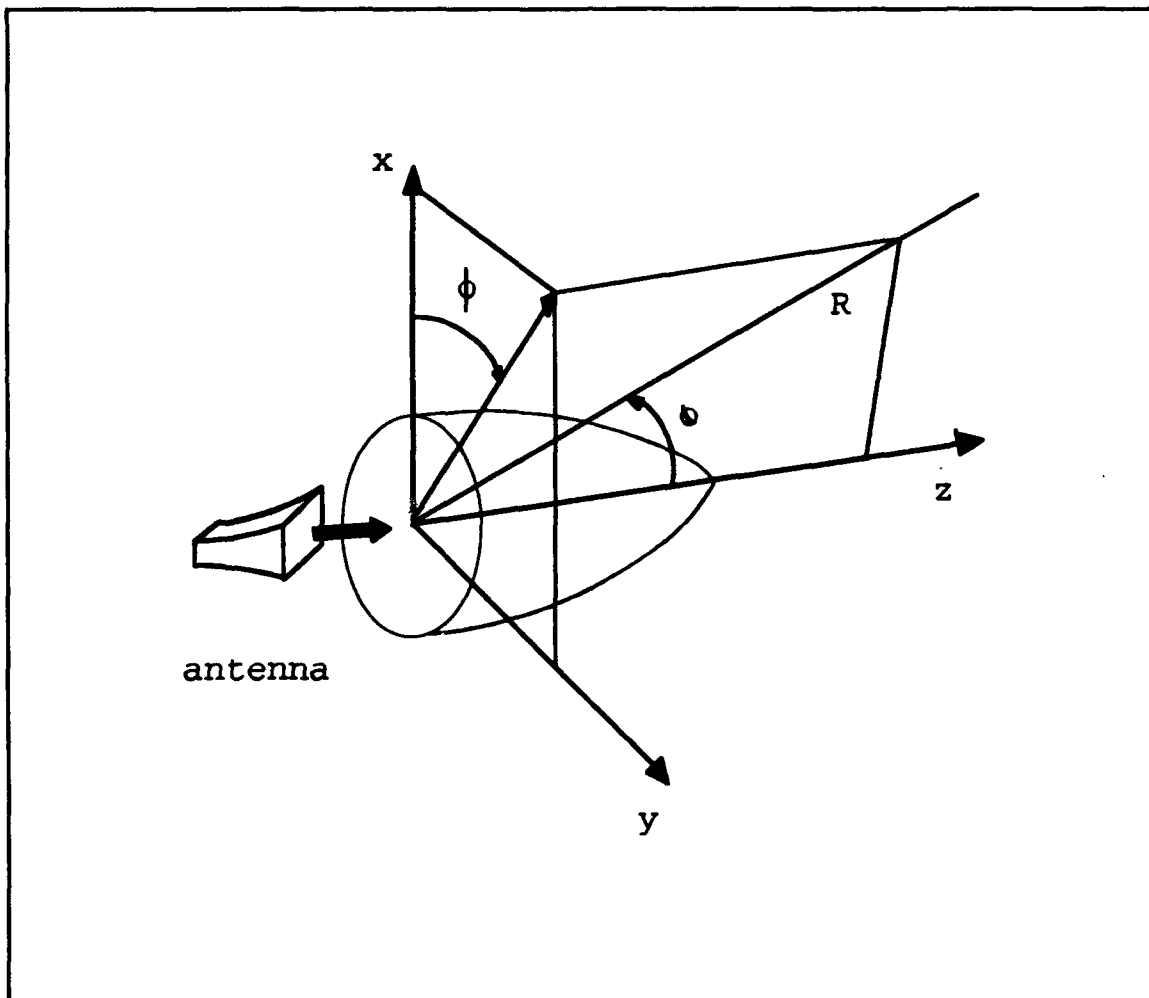

Figure 5.1 Spherical coordinate system.

The pattern can be determined from the total electric field in the direction of the observation point (θ, ϕ). By calculating the electric field due to the currents on the antenna, and the electric field due to the currents on the radome, the total electric field can be determined by summing the two. Changes in the initial current distribution caused by scattering back from the radome toward the antenna are neglected. The scattering back toward the antenna primarily affects the VSWR looking into the antenna terminals. This is small as verified by the VSWR measurement in Chapter IV. [Ref. 2: p. 5]

Assuming a lossless antenna, the terms gain and directivity will be used interchangeably. Used in this context, gain is a measure of the ability to concentrate power in a particular direction. The term G_o is the maximum value of the gain and is defined as the ratio of maximum radiation intensity to the average radiation intensity

$$G_o = \frac{4\pi U(\theta, \phi)}{\oint U(\theta, \phi)\, d\Omega} \, . \qquad (5.1)$$

$U(\theta, \phi)$ is the radiation intensity and $d\Omega = \sin\theta\, d\theta\, d\phi$ is the differential solid angle. [Ref. 11: pp. 29-43]

The radiation intensity for an antenna in a particular direction is the power radiated per unit solid angle, and is proportional to the magnitude of the electric field squared.

$\mathbf{E}$ is the sum of $\mathbf{E}^a$ (electric field of the antenna) and $\mathbf{E}^s$ (the electric field scattered by the radome). Therefore the radiation intensity is given by

$$U(\theta,\phi) = \frac{1}{2\eta_o}|E(\theta,\phi)|^2 \ .$$
(5.2)

[Ref. 2: p. 6]

A. COMPUTER MODELING

The computer model used to compute the antenna and radome pattern and gain was developed by Francis [Ref. 1]. It is based on a method of moments (MM) solution for rotationally symmetric radomes that has been modified to handle thin-shell dielectric radomes. The model is an extension of the Mautz and Harrington body of revolution code [Ref. 3]. The original code as developed by Francis had several limitations, but its capabilities were extended by Klopp [Ref. 2]. A summary of the computer code capabilities and limitations is given in Table 5.1 and 5.2.

TABLE 5.1. COMPUTER CODE CAPABILITIES

CAPABILITIES	
Circular or rectangular aperture	Arbitrary BOR shape
Arbitrary amplitude and phase distribution	Step approximation to inhomogeneous radomes
All antenna near field terms included	Step approximation to variations in thickness

31

TABLE 5.2.   COMPUTER CODE CAPABILITIES

RESTRICTIONS/LIMITATIONS	
Radome is "thin" electrically	Radome properties represented by a complex surface impedance
Phase scanning only (no gimballed antenna)	Restricted to moderate radome sizes due to computer memory limitations
Ohmic loss inside of the radome not included	

1.   METHOD OF MOMENTS

MM is a numerical procedure for solving the E-field integral equation (EFIE) for the unknown current $\mathbf{J}$. In this section a brief summary of the MM solution will be presented. A more detailed derivation can be found in [Ref. 3].

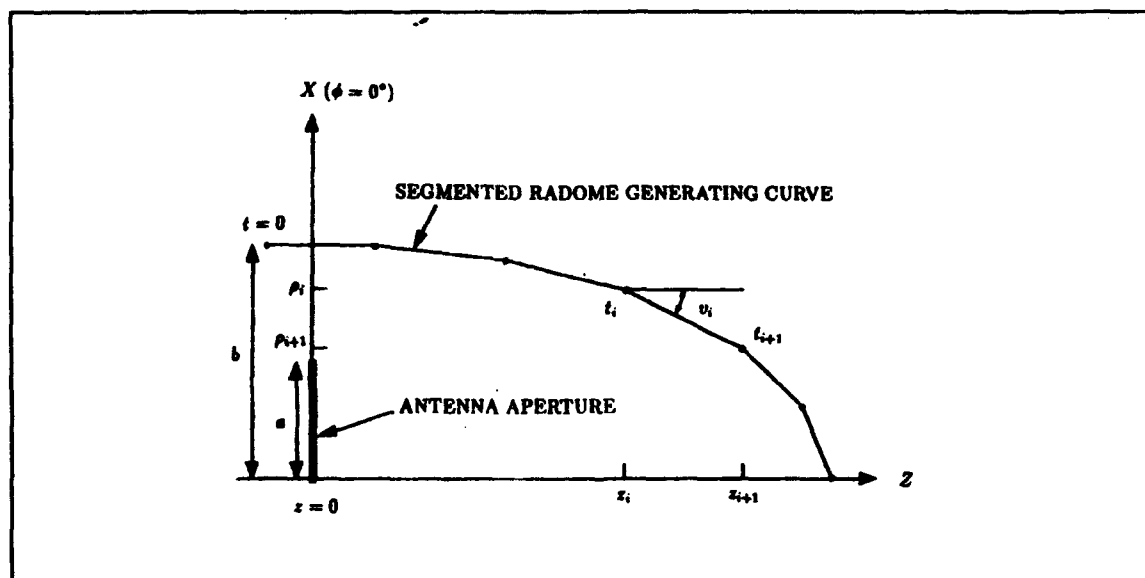To begin with, the radome curve is discretized as shown in Figure 5.2.   The surface is treated as perfect

Figure 5.2 Discretized radome.

conductor with a correction term to account for the dielectric material properties to be added later. On the surface, the MM current basis functions are:

$$\mathcal{J}^t_{ni} = \hat{t}\frac{T_i(t)}{\rho}e^{-jn\phi} \quad n=0,\pm 1,\ldots\pm\infty \quad i=1,2\ldots,N_s-2 \quad \textbf{(5.3)}$$

$$\mathcal{J}^\phi_{ni} = \hat{\phi}\frac{P_i(t)}{\rho}e^{-jn\phi} \quad n=0,\pm 1,\ldots\pm\infty \quad i=1,2\ldots,N_s-1 \quad . \quad \textbf{(5.4)}$$

$T_i(t)$ is a triangle function extending over two segments, and $P_i(t)$ is a pulse function extending over a single segment. These functions are shown in Figure 5.3. The unit vectors $\hat{t}$ and $\hat{\phi}$ are in the radial and azimuthal directions. The variable t is the arclength along the generating curve of the BOR, and the variable ρ is the distance of a point from the z axis. N_s is the number of surface generating points. Thus, the electric current $\mathcal{J}_s$ on the surface is represented by

$$\mathcal{J}_s = \sum_{n=-\infty}^{\infty}\left[\sum_{p=1}^{N_s-2} I^t_{pn}\mathcal{J}^t_{pn} + \sum_{q=1}^{N_s-1} I^\phi_{qn}\mathcal{J}^\phi_{qn}\right] . \qquad \textbf{(5.5)}$$

The MM testing procedure (Galerkin's Method) reduces the EFIE to a matrix equation for the unknown coefficients for each azimuthal mode, I_n

$$I_n = Z_n^{-1}V_n . \qquad \textbf{(5.6)}$$

33
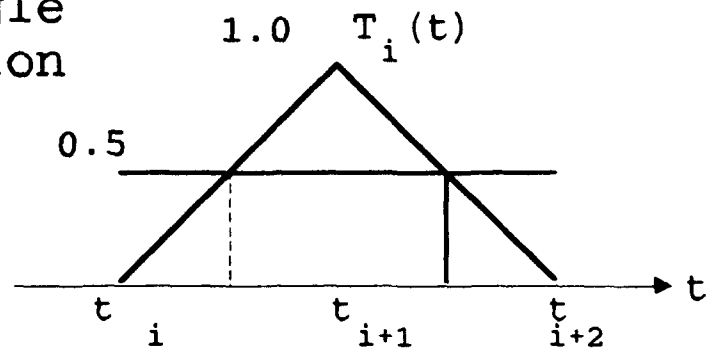
Figure 5.3 Basis functions: pulse (P) and triangle (T).
[From Ref. 1]

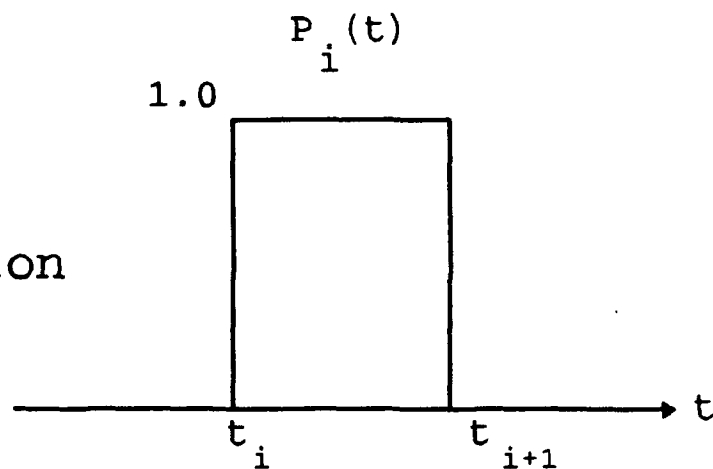Z_n is a square matrix called the impedance matrix for mode n, which can be partitioned into blocks corresponding to the vector directions $\hat{t}$ and $\hat{\phi}$

$$Z_n = \begin{bmatrix} Z_n^{tt} & Z_n^{t\phi} \\ Z_n^{\phi\phi} & Z_n^{\phi\phi} \end{bmatrix} . \tag{5.7}$$

The test function direction is indicated by the first superscript, and the expansion function direction by the second superscript. V_n is a column vector called the excitation vector. Its elements are determined from the electric field on the surface of the radome, and will be discussed in more detail later. Detailed expressions for the elements of Z are given in [Ref. 1].

2. THIN SHELL APPROXIMATION

To account for the fact that the radome material is a dielectric rather than a conductor, a correction term (Z_{L_n}) is added to the MM impedance matrix

$$Z_n = Z_{MM_n} + Z_{L_n} . \tag{5.8}$$

Z_{MM} is the MM impedance matrix for the perfectly conducting surface. The elements of Z_{L_n} are determined from

$$[Z_L]_{i1n}^{pq} = \int_s \int \underline{W}_{in}^p \cdot \underline{J}_{1n}^q Z_s ds \quad (p, q = t, \phi) \tag{5.9}$$

35

or, because of the orthogonality of $\hat{t}$ and $\hat{\phi}$

$$[Z_L]_{i1n}^{pp} = \int_s \int \vec{W}_{in}^p \cdot \vec{J}_{1n}^p Z_s ds. \tag{5.10}$$

The functions $\vec{W}_n$ are the MM testing functions used to obtain equation (5.7). For Galerkin's method they are the complex conjugates of the expansion functions $\vec{J}_n$. Due to the choice of triangles in t and pulses in ϕ, the correction matrix will be diagonal for the $Z^{\phi\phi}$ block of equation (5.7) and tridiagonal for the Z^t block.

The radome surface impedance is given by

$$Z_s = \frac{1}{j\omega (\epsilon - \epsilon_o) t} \tag{5.11}$$

where t in this case is the thickness of the shell. It can be rewritten in terms of the dielectric constant (ϵ), thickness in wavelengths ratio $(n\lambda)$, and the loss tangent (tan δ)

$$Z_s = \frac{60}{n\lambda[j(\epsilon_r - 1) + \epsilon_r \tan\delta]}. \tag{5.12}$$

This equation is based on a solid homogeneous radome material of constant thickness. Multi-layered radomes can be modeled as a solid material by using an equivalent dielectric constant. This is the approach used to model the three layered HARM radome wall. For radomes with variations in

36

thickness and dielectric constant, the surface can be analyzed by a stepped index and thickness. On each segment of the radome curve, ϵ_r, $\tan \delta$, and t can be specified independently.

3. DETERMINING THE EXCITATION VECTOR

To compute the excitation vector $\underline{V}$ of (5.6), the electric field of the antenna $\underline{E}$ must be known, and it can be determined by integrating the known current $\underline{J}_i$ on the antenna. The excitation elements are

$$\underline{V}_{in}^p = \int\int_{s_a} \underline{W}_{in}^p \cdot \underline{E}^a \, ds \qquad (p=t,\phi) . \tag{5.13}$$

For a x polarized uniformly excited aperture lying in the xy plane, with a linear phase applied to scan the beam in the direction θ_s ($\phi_s=0$),

$$\underline{J}_i = \hat{x} J_o e^{-jkx'\sin\theta_s} . \tag{5.14}$$

The following expressions are the Cartesian components of the radiated electric field

$$E_x^a = \frac{-j\eta_0 J_0}{4\pi k} \int_{s_a}\int [G_1 + (\rho\cos\phi - \rho'\cos\phi')^2 G_2] \tag{5.15}$$
$$\cdot e^{jk(\rho'\cos\phi'\sin\theta_s - R)} \rho' d\rho' d\theta'$$

37

$$E_y^a = \frac{-j\eta_0 J_0}{4\pi k} \int_{S_a}\int (\rho\cos\phi - \rho'\cos\phi')(\rho\sin\phi - \rho'\sin\phi')$$
$$\cdot\, G_2 e^{jk(\rho'\cos\phi'\sin\theta_s - R)} \rho'd\rho'd\theta' \tag{5.16}$$

$$E_z^a = \frac{-j\eta_0 J_0}{4\pi k} \int_{S_a}\int (\rho\cos\phi - \rho'\cos\phi')^2$$
$$\cdot\, zG_2 e^{jk(\rho'\cos\phi'\sin\theta_s - R)} \rho'd\rho'd\phi' \,. \tag{5.17}$$

Primed quantities are associated with the antenna; unprimed quantities with the observation point (radome). The distance between the two points is

$$R = \sqrt{(\rho-\rho')^2 + z^2 + 4\rho\rho'\sin^2\left(\frac{\phi-\phi'}{2}\right)} \,. \tag{5.18}$$

Also used in (5.15) through (5.17) are

$$G_1 = \frac{k^2R^2 - 1 - jkR}{R^3} \tag{5.19}$$

$$G_2 = \frac{3 + 3jkR - k^2R^2}{R^5} \,, \tag{5.20}$$

where $k = 2\pi/\lambda$.

The rectangular components of the electric field are then converted to spherical components by using the

transformation

$$E_r^a = E_x^a \sin\theta\cos\phi + E_y^a \sin\theta\sin\phi + E_z^a \cos\theta$$

$$E_\theta^a = E_x^a \cos\theta\cos\phi + E_y^a \cos\theta\sin\phi - E_z^a \sin\theta \qquad (5.21)$$

$$E_\phi^a = -E_x^a \sin\phi + E_y^a \cos\phi \ .$$

Finally, the spherical components from equation (5.13) can be used to generate the excitation elements by numerically integrating equation (5.13)

$$V_{ni}^t = \int_0^{2\pi} \int_{t_i}^{t_{i+2}} T_i(t) e^{-jn\phi}$$
$$\cdot \left[\sin(v_i - \theta) E_\theta^a + \cos(v_i - \theta) E_r^a \right] dt d\phi \qquad (5.22)$$

$$V_{ni}^\phi = \int_0^{2\pi} \int_{t_i}^{t_{i+1}} P_i(t) e^{-jn\phi} E_\phi^a \frac{\rho}{\rho_i} \ dt d\phi \ . \qquad (5.23)$$

It will be assumed that the antenna radiated field in the rear hemisphere ($\theta > 90^\circ$) is zero.[Ref. 12: pp. 1-6]

39

VI. DATA ANALYSIS

A. COMPUTER PROGRAMS

The mathematical theory presented in Chapter V is encoded in FORTRAN and run on a Sun SPARCstation™ under UNIX. Two programs are used to compute and plot the pattern and gain calculations: RADOME.F and GAIN.F.

1. RADOME.F

The program RADOME.F was originally developed by Francis [Ref. 1] and called LDBORMM.F. It determined the series expansion coefficients of the current J_s induced on the surface of the radome, and also the total electric field at an observation point. It was modified by Klopp [Ref. 2] to take advantage of symmetry allowing the antenna mainbeam to scan in both θ and ϕ.

The program is interactive, prompting the user for various radome, antenna and calculation parameters. The output from the program is two ASCII files. **Outldbor** is a listing of the specific radome and calculation parameters. It includes the input parameters, radome geometry and impedance, and a table of the pattern magnitude and phase. **Curcoefsdat** is a file containing the current expansion coefficients as well as geometry data. MATLAB™ formatted files for plotting the θ and ϕ components of the electric field are also generated.

The subroutine "TAPER" in RADOME.F was modified to include a cosine amplitude distribution to approximate the actual horn aperture distribution. A quadratic phase error was also added in the H-plane as discussed later.

2. GAIN.F

The output file **curcoefsdat** from RADOME.F is used by GAIN.F along with files of gaussian integration constants. According to equation (5.1), the electric field is integrated over all space to obtain the gain of the system. An output file named **outint** is generated which contains the calculation parameters and results. [Ref. 2: pp. 36-45]

B. COMPUTED AND MEASURED RESULTS

The program RADOME.F was used to compute the antenna pattern for the 56X1 antenna without the radome. Figures 6.1 and 6.3 show the computer generated plots for the E and H-plane patterns respectively. The horn aperture dimensions are 1.8λ in the E-plane (xz) and 2.6λ in the H-plane (yz). Plots of the antenna with the radome were then obtained for both the E and H-planes, and are shown in Figures 6.5 and 6.7. Gain was computed for all plots and the results are summarized in Tables 6.1 and 6.2.

Measured pattern plots for the antenna are shown in Figures 6.2 and 6.4. E and H-plane patterns with the radome are shown in Figures 6.6 and 6.8. In all cases f = 10 GHz. From equation (3.2), the radome impedance is $Z = 218 - j133$.

41

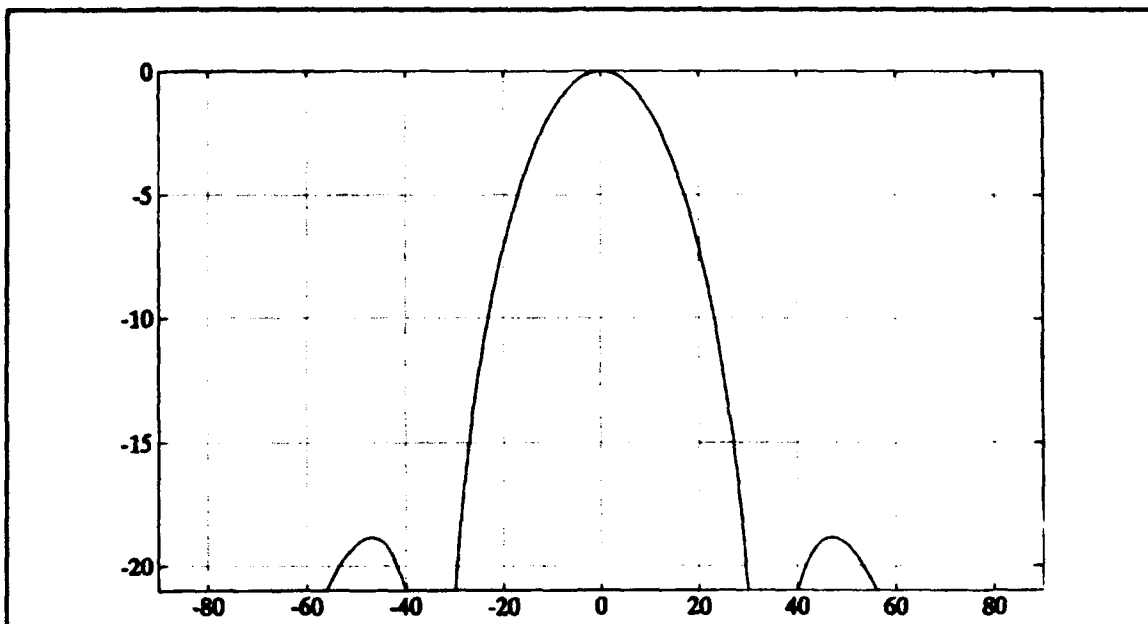**Figure 6.1** Calculated pattern plot of the 56X1 antenna in the E-plane. Vertical scale in dB and the horizontal scale in degrees.
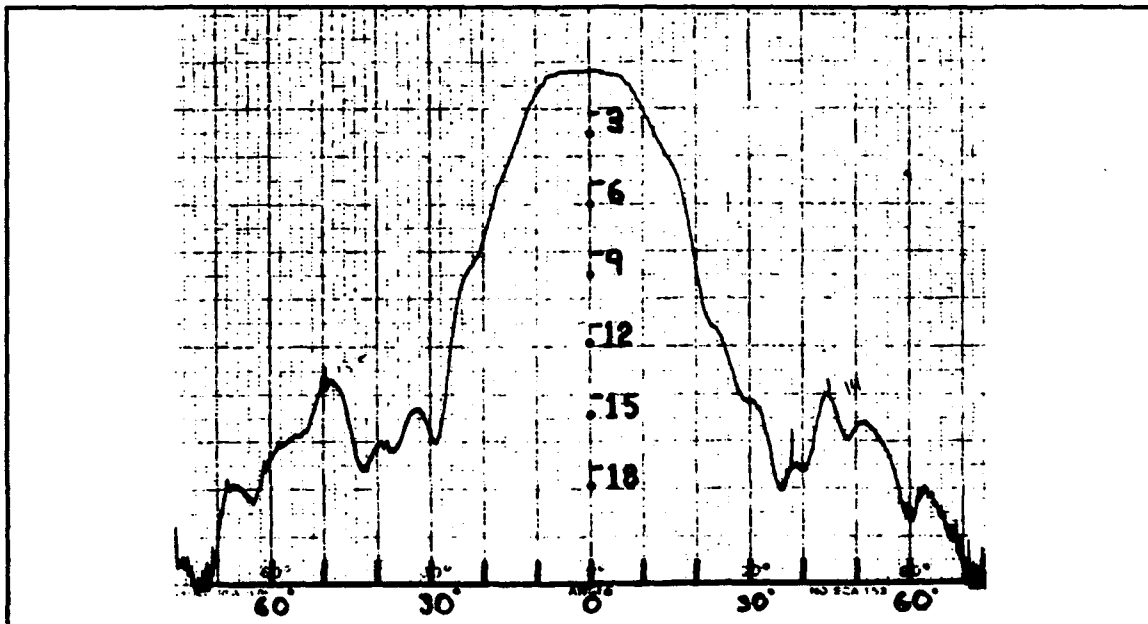
Figure 6.2 Measured pattern of the 56X1 antenna in the E-plane. Vertical scale in dB and the horizontal scale in degrees.

42
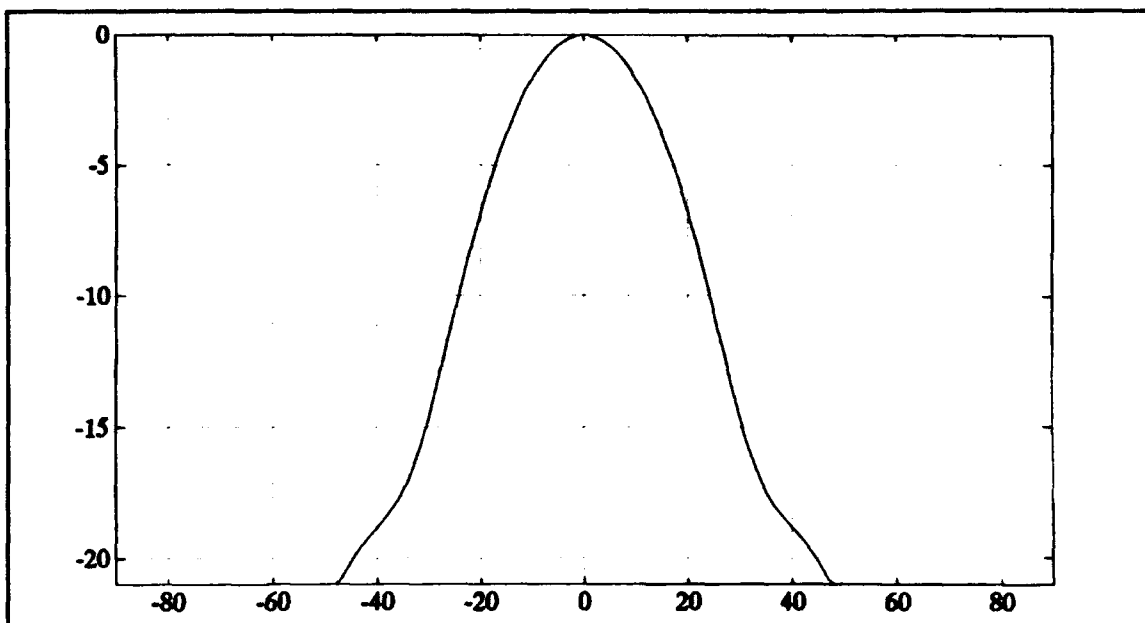
Figure 6.3 Calculated pattern of the 56X1 antenna in the H-plane.

Figure 6.4 Measured pattern of the 56X1 antenna in the H-plane.
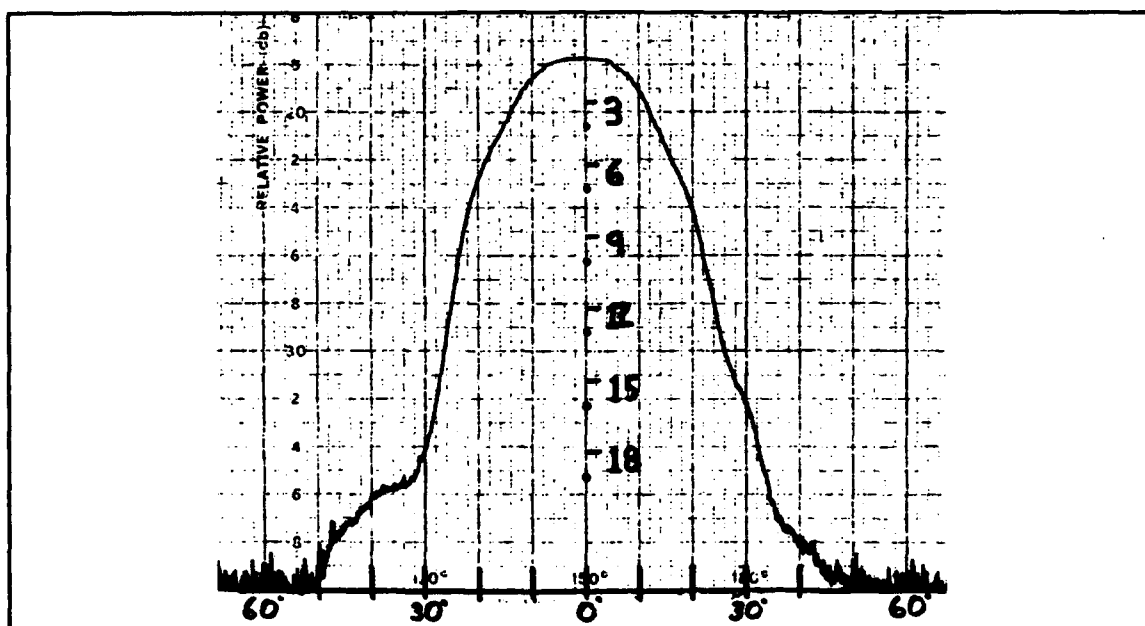
Figure 6.5 Calculated pattern of the HARM radome and 56X1 antenna in the E-plane.

Figure 6.6 Measured pattern of the HARM radome and 56X1 antenna in the E-plane.
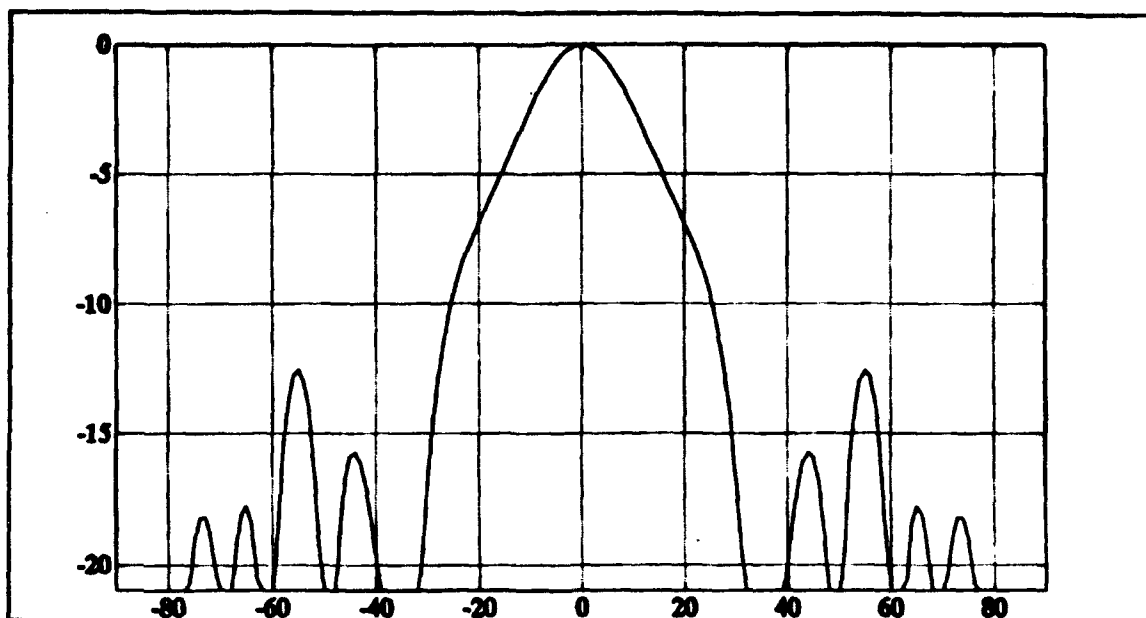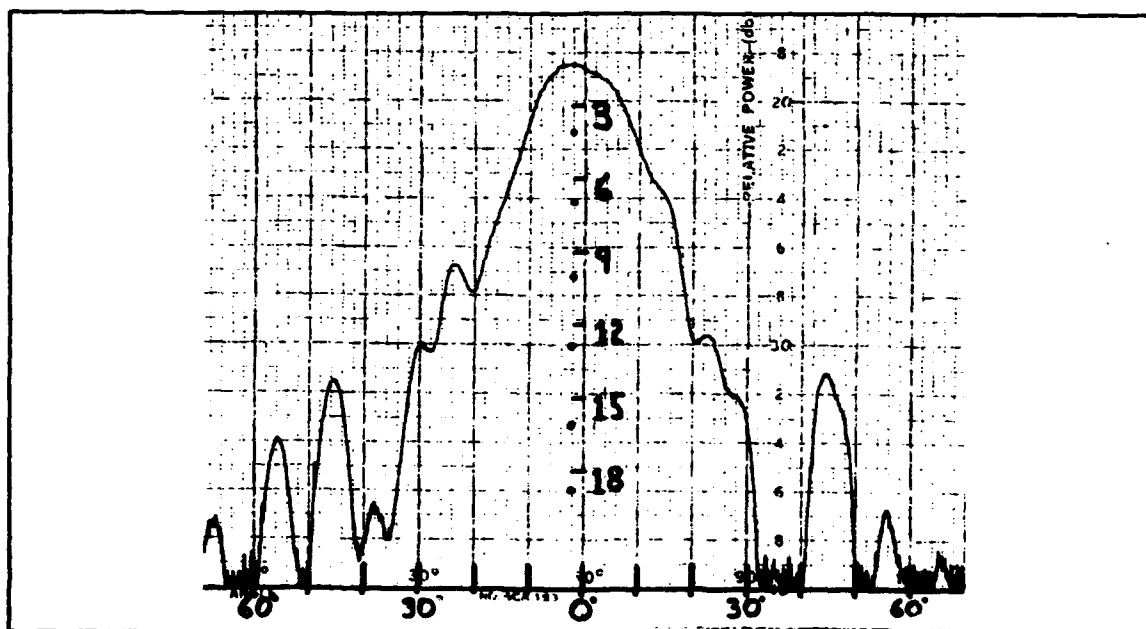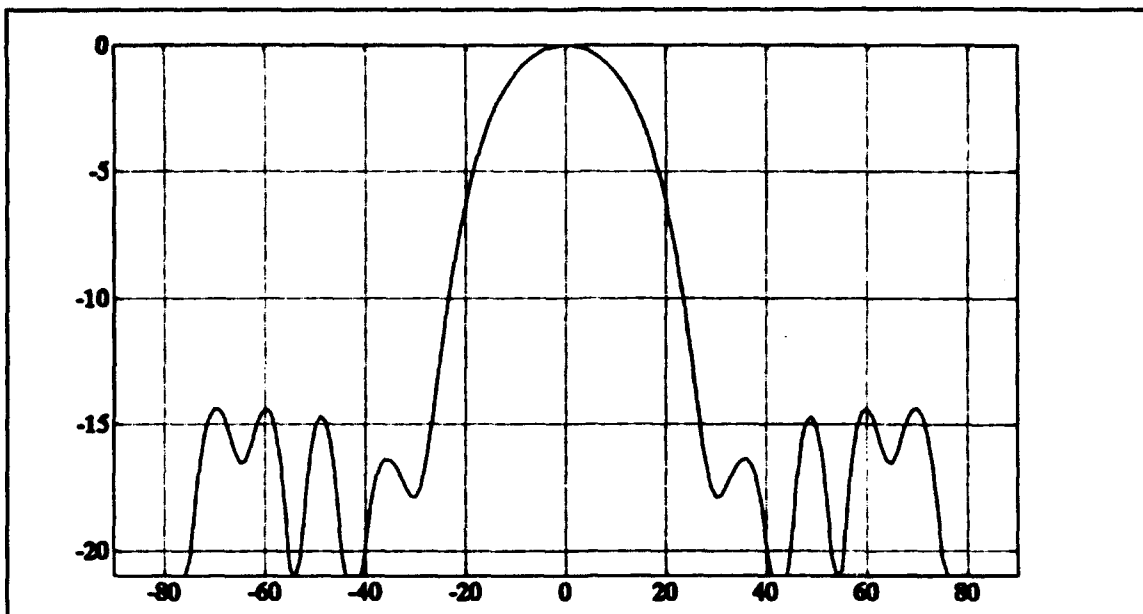
44

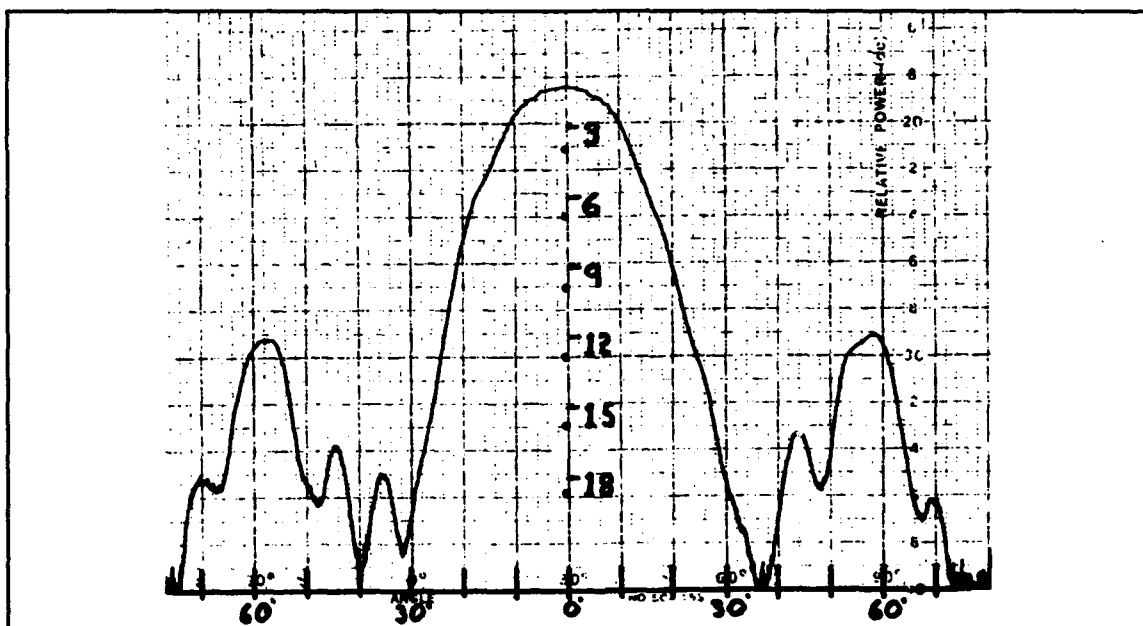**Figure 6.7** Calculated pattern of the HARM radome and 56X1 antenna in the H-plane.

Figure 6.8 Measured pattern of the HARM radome and 56X1 antenna in the H-plane.

45

TABLE 6.1   MAINLOBE GAIN MEASUREMENTS (E-PLANE)

	56X1 ANTENNA	56X1 & HARM RADOME
E-PLANE (COMPUTED)	17.04 dB	15.97 dB
E-plane (MEASURED)	17.00 dB ± 0.3 dB	16.70 dB ± 0.3 dB

TABLE 6.2   MAINLOBE GAIN MEASUREMENTS (H-PLANE)

	56X1 ANTENNA	56X1 & HARM RADOME
H-PLANE (COMPUTED)	17.04 dB	15.97 dB
H-plane (MEASURED)	17.00 dB ± 0.3 dB	16.40 dB ± 0.3 dB

In the code a rectangular aperture of dimensions a = 1.8λ and b = 2.6λ was used to approximate the horn aperture. The amplitude distribution was assumed to be a cosine and a quadratic phase error was also added to the H-plane (y direction). Thus the aperture field is of the form

$$E(x,y) \approx \hat{x}\cos\left(\frac{\pi y}{b}\right) e^{j(\frac{2y}{b})^2 \, 70°}$$ (6.1)

The measured and computed data is generally in good agreement. The estimated accuracy of the gain measurement is 0.3 dB. In general the sidelobe levels and position are within a few dB. No background subtraction capability currently exists in the system. Some of the sidelobe difference can be attributed to chamber reflections. This is

evident from the asymmetry in the measured patterns.

Variations in the impedance had little effect on the computed pattern sidelobe levels. The radiation patterns for three impedance values are shown in Figure 6.9.
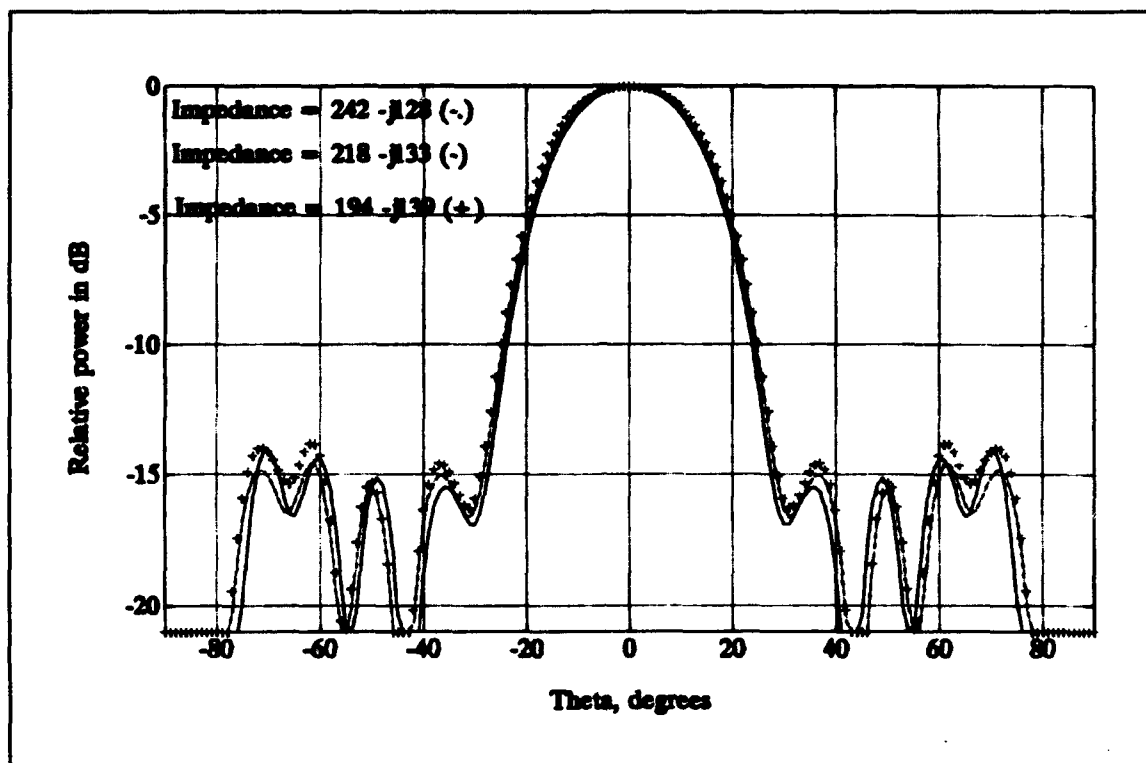

Figure 6.9 H-plane plot of the HARM radome with three different impedances showing little variation in the sidelobe gain levels.

VII. CONCLUSION

A. SUMMARY OF RESULTS

The computer generated data for the HARM radome verifies that the programs RADOME.F and GAIN.F agree with measured results from the anechoic chamber. Typical input values for the computer code are listed in Appendix A.

The antenna was modelled as a rectangular aperture with a cosine amplitude distribution in the H-plane. A quadratic phase error was also added in the H-plane to fill in the first null and broaden the main beam. As expected, the patterns with the radome have higher sidelobes when compared to the antenna alone. This is due to the ogive shape which reflects energy towards other parts of the radome surface. The resulting multiple reflections result in many sidelobes at wide angles from the mainlobe of the antenna. In general the sidelobe characteristics of the computed and measured patterns were similar.

The gain predictions were also fairly close in agreement with measured data. Repeatability and stability was a problem with the measured gain because of equipment problems. Also no background subtraction capability exists and therefore chamber reflections were present. Another potential source of error is due to boresighting the antenna and radome. The alignment was simply done "by eye" and is only accurate to a couple of

degrees. Also, the data in Table 6.1 assumes that the mismatch loss is the same for the antenna with and without the radome. With all of these factors taken into account the measured and computed gain data were within 0.5 dB of each other, which is about the measurement accuracy of the NPS anechoic chamber.

B. RECOMMENDATIONS

Listed below are the following suggestions for further research:

1. Perform additional measurements of other missile radomes and compare with the predictions of the computer model;

2. Vary the antenna type to determine its effect on the radiation pattern and code accuracy;

3. Incorporate a new and more accurate measurement system into the Naval Postgraduate School anechoic chamber in order to provide more repeatable data;

4. Extend the study to include other frequency bands;

5. Investigate other radome shapes and materials.

This thesis showed that the programs RADOME.F and GAIN.F provided accurate estimates for the radiated patterns for the HARM radome. As a design tool, it has the potential to reduce cost and development time for future radome designs.

APPENDIX A. INPUT DATA FOR RADOME.F

A. INPUT DATA FOR 56X1 ANTENNA

This appendix lists the data file used to compute the 56X1 antenna pattern. The program RADOME.F is used, but a "microscopic" disc is entered as the radome. Thus the scattered field is zero and only the antenna pattern results.

TABLE A.1.   INPUT DATA FOR E-PLANE AND H-PLANE

	E-PLANE	H-PLANE
LETTER CODE FOR FILE	a	b
BOR GEOMETRY	4 (DISK)	4 (DISK)
DISK RADIUS	0.001	0.001
NUMBER OF POINTS	3	3
FILENAME IN T (NT)	gaus2	gaus2
FILENAME IN PHI (NPHI)	gaus12	gaus12
FILENAME ANTENNA INTEGRATION (NANT)	gaus20	gaus20
PLOTTING INCREMENT	1	1
HIGHEST MODE	5	5
PHI IN DEGREES	0	90
SCAN ANGLE	0,0	0,0
COMPLEX IMPEDANCE	(400,0)	(400,0)
ARAD,BRAD	1.8,2.6	1.8,2.6

B.   INPUT DATA FOR AGM-88 HARM RADOME

This appendix lists a typical RADOME.F data file.

TABLE A.2.   INPUT DATA FOR E-PLANE AND H-PLANE

	E-PLANE	H-PLANE
LETTER CODE FOR FILE	c	d
BOR GEOMETRY	1 (OGIVE)	1 (OGIVE)
SURFACE CURVATURE	12.5	12.5
ZPRIME	0.5	0.5
BASE RADIUS	2.65	2.65
FILENAME IN T (NT)	gaus2	gaus2
FILENAME IN PHI (NPHI)	gaus20	gaus20
FILENAME ANTENNA INTEGRATION (NANT)	gaus12	gaus12
PLOTTING INCREMENT	1	1
HIGHEST MODE	10	10
PHI IN DEGREES	0	90
SCAN ANGLE	0,0	0,0
COMPLEX IMPEDANCE	(218,-133)	(218,-133)
ARAD,BRAD	1.8,2.6	1.8,2.6

APPENDIX B. INPUT DATA FOR GAIN.F

A. INPUT DATA FOR ANTENNA GAIN

This appendix lists the input file for the antenna gain calculation.

TABLE B.1.   INPUT DATA FOR E-PLANE AND H-PLANE

	E-PLANE	H-PLANE
FILENAME IN PHI (NPHI)	gaus12	gaus12
LETTER CODE FOR FILE CURCOEFSDAT	same as used in RADOME.F	same as used in RADOME.F
FILENAME FOR ANTENNA INTEGRATION	gaus20	gaus20
THETA START AND STOP ANGLES	0,180	0,180
PHI START AND STOP ANGLES	0,180	0,180

B.   INPUT DATA FOR RADOME GAIN

This appendix lists the input file for the antenna and radome gain calculation.

TABLE B.1.   INPUT DATA FOR E-PLANE AND H-PLANE

	E-PLANE	H-PLANE
FILENAME IN PHI (NPHI)	gaus20	gaus20
LETTER CODE FOR FILE CURCOEFSDAT	same as used in RADOME.F	same as used in RADOME.F
FILENAME FOR ANTENNA INTEGRATION	gaus12	gaus12
THETA START AND STOP ANGLES	0,180	0,180
PHI START AND STOP ANGLES	0,180	0,180

APPENDIX C. CODE FOR RADOME IMPEDANCE

```
!del impedan1.met
clear
% compute equivalent radome surface impedance
f1=8.;
f2=12.;
fstep=.1;
m=0;
for f=f1:fstep:f2
m=m+1;
w=3e8/f/1e9;
%thickness of each region
d1=.054*.0254;
d2=.12*.0254;
d3=.03*.0254;
% relative dielectric constants
er1=3.5;
er2=1.2;
er3=3.5;
k=2.*pi/w;
% assume lossless radome materials (alpha=alpha2=alpha3=0).
Find betas.
a1=0.;
a2=0.;
a3=0.;
b1=k*sqrt(er1);
b2=k*sqrt(er2);
b3=k*sqrt(er3);
g1=a1+j*b1;
g2=a2+j*b2;
g3=a3+j*b3;
% characteristic impedance of each section
z0=377.;
z1=z0*sqrt(1./er1);
z2=z0*sqrt(1./er2);
z3=z0*sqrt(1./er3);
% impedance looking into each boundary
zc=z3*(z0+z2*tanh(g3*d3))/(z3+z0*tanh(g3*d3));
zb=z2*(zc+z2*tanh(g2*d2))/(z2+zc*tanh(g2*d2));
za=z1*(zc+z1*tanh(g1*d1))/(z1+zb*tanh(g1*d1));
% reflection coefficient at the input
%R(m)=((za-z0)/(za+z0));
R(m)=za;
M(m)=abs(R(m));
F(m)=f;
Re(m)=real(R(m));
Im(m)=imag(R(m));
P(m)=atan2(Im(m),Re(m))*180./pi;
```

```
end
tplot(F,R),grid
plot(F,M);
grid
meta impedan1.met;
pause
plot(F,P);
grid
meta
pause
```

LIST OF REFERENCES

1. Francis, R. M., "A Computer Model for the Transmission Characteristics of Dielectric Radomes", Master's Thesis, Naval Postgraduate School, Monterey, California, March 1992.

2. Klopp, K. A., "Antenna Gain Loss and Pattern Degradation due to Transmission Through Dielectric Radomes", Master's Thesis, Naval Postgraduate School, Monterey, California, pp. 5-6, 36-45, March 1993.

3. Mautz, Joseph R. and Harrington, Roger F., "An Improved E-Field Solution for a Conducting Body of Revolution," Technical Report no. TR-80-2, Syracuse University, Syracuse, New York, January 1980.

4. Walton, J. D., _Radome Engineering_, pp. 1-3, 44-48, Marcel Dekker, Inc, 1970.

5. Lennox, Duncan S., and Rees, Arthur, _Janes's Air-Launched Weapons_, JALW-ISSUE 3, Janes's Information Group, U.K., 1989

6. Schleher, D. Curtis, _Introduction to Electronic Warfare_, pp. 18-23, Artech House Inc., 1986.

7. Naval Electronics Laboratory Center Report TR2023, "Radome Development for a Broadband RF Missile Sensor", by F. D. Groutage, pp. 1-4, 16-18, 25 January 1977.

8. Facsimile from Mosko, Joseph A., Code C28203, NAWCWPNS, pp. 1-5, 22 April 1993.

9. Cheng, David K., _Field and Wave Electromagnetics_, pp. 454-467, Addison-Wesley Publishing Company, December 1990

10. _HP8510C Network Analyzer_, pp. (3-1)-(3-8), (10-1)-(10-4), Hewlett Packard Co., Santa Rosa, California, June 1991.

11. Balanis, Constantine A., _Anetnna Theory_, pp. 29-43, John Wiley & Sons, Inc., 1982.

12. Jenn, D. C., Francis, R. M., and Klopp, K. A., "Computer Model for Axially Symmetric Dielectric Radomes in the Near Field of a Circular Aperture", unpublished paper, Naval Postgraduate School, Monterey, California. pp. 1-6.

57

INITIAL DISTRIBUTION LIST

No. copies

1. Defense Technical Information Center (DTIC)   2
   Cameron Station
   Alexandria, VA. 22304-6145

2. Library, Code 52   2
   Naval Postgraduate School
   Monterey, CA 93943-5002

3. Director, Space and Electronic Combat Division (N64)   1
   Space and Electronic Warfare Directorate
   Chief of Naval Operations
   Washington DC 20350-2000

4. Professor D.C. Jenn, Code EC/Jn   2
   Department of Electrical and Computer Engineering
   Naval Postgraduate School
   Monterey, CA 93943-5000

5. Joseph A. Mosko, NAWCWPNS CodeC28203   1
   Microwave Components Consultant
   China Lake, CA 93555-6001

6. Lieutenant D.C. Chang   1
   COMPHIBGRU ONE
   FPO AP 96601-6006

7. Professor R. Janaswamy, Code EC/JS   1
   Department of Electrical and Computer Engineering
   Naval Postgraduate School
   Monterey, CA 93943-5000

8. Chairman, Electronic Warfare Academic Group   1
   Code EW
   Naval Postgraduate School
   Monterey, CA 93943-5000